上海科技大学
ShanghaiTech University

本科毕业论文（设计）

题　　目：	高迁移率半导体材料电磁性质研究
学生姓名：	高鸿翔
学　　号：	18797306
入学年份：	2014年
所在学院：	信息科学与技术学院
指导教师：	寇煦丰 教授
攻读专业：	电子信息工程

上海科技大学教学事务处 制

二零一　　年　　月

上海科技大学
ShanghaiTech University

Bachelor's Thesis

Topic:	Electromagnetic Properties of High Mobility Semiconductors
Student Name:	Gao Hongxiang
Student ID:	18797306
Year of Attendance:	2014
Department:	School of Information Science and Technology
Advisor:	Prof. Kou Xufeng
Major:	Electrical and Electronic Engineering

Made by Office of Academic Affairs, ShanghaiTech University
Date: / /

摘要

提到近几十年来电子产品性能的发展趋势，许多人首先会想到的便是摩尔定律。其核心内容大致为：当价格保持不变的情况下，集成电路上可以容纳的元器件的数目每隔18至24个月便会增加一倍。自1965年被提出以来，摩尔定律的预测几乎能够一直吻合电脑处理器中晶体管的数量，甚至可以说，现代电子芯片产业就是根据摩尔定律的预测进行不断更新的。然而，近些年来，随着制造工艺上遇到了瓶颈，摩尔定律也迎来了它的挑战。由于芯片尺寸不断减小，随着量子力学效应的产生，一些器件不再能够以简单的半导体物理知识加以分析，并会影响器件本身的性能。这使芯片的设计的难度大大地增加了。因此，进一步探索高迁移率的半导体材料成为了一项重要的任务。相比于传统的半导体材料，具有高迁移率性质的半导体材料会表现出许多新的现象和性质。本文提供了一种对于具有高迁移率的半导体电磁性质的测量方法和物理模型，从而能够更好地描述该半导体的物理性质。

对于传统半导体来说，通常只有电子或空穴一种载流子在参与导电并且一般工作在小霍尔角的情况下，而对于高迁移率半导体来说，参与导电的可能有两种载流子且可能工作在大霍尔角的条件。因此为了能够更好地描述其物理性质，需要提供新的在大霍尔角情况下双载流子共同作用下的物理模型。本文通过针对这一问题的研究，归纳了可以同时符合高迁移率半导体和传统半导体的模型。同时，以新型高迁移率半导体材料Cd_3As_2为例，通过Oxford低温电磁学性质测量设备对该材料性质进行测量之后，获得了该材料在不同温度和磁场条件下的磁阻以及霍尔电阻的阻值。经过之前所获得的物理模型拟合和验证之后，我们发现，在处于2.1K的低温条件下时，Cd_3As_2能够提供高达3.4×10^4cm/V·s的高迁移率。进一步的，本文对该材料进行了量子振荡现象方面的研究。

关键词：大霍尔角，双载流子模型，Cd_3As_2材料，量子振荡现象

ABSTRACT

When talking about the trend in development of electronic products in recent decades, Moore's law is the first thing that people would think of. Its core content is the complexity of integrated circuits, with respect to minimum component cost, doubles every 18 to 24 months. Since it was proposed in 1965, Moore's law could almost fit the number of tubes in chips, to some extent, the development of modern electronic industry was following the forecast of Moore's law. However, with the bottlenecks in the development of fabrication process, Moore's law is challenged. Quantum effects need to be taken into account since the scale of components is in quantum scale and we can not analyze them easily with traditional semiconductor physics. Finding semiconductor materials with high mobility becomes an important task. Compared with traditional materials, semiconductor materials with high mobility will show novel properties and phenomenon. This work provides a general approach and physical model to investigate semiconductor materials with high mobility and therefore gives a more exact description of their physical properties.

For traditional semiconductors, they usually work with small hall angles and there is only one kind of carriers that participate the conduction process. However, for semiconductor with high mobility, there may be two kinds of carriers that are pariticipating in the conduction process and in some cases, they are working with large hall angles. To give a better description of these materials, a new physical model which takes large hall angle and two-band carriers into account is needed. This paper gives a generic model that can fits both traditional and new materials. And taking the Cd_3As_2, a new kind of semiconductor material with high mobility as an example, we measured its magnetoresistance and hall resistance at different magnetic fields and temperature by Oxford system. After verification and fitting the physical model, we find that Cd_3As_2 give rise to a high electron mobility of 3.4×10^4cm/V·s at 2.1K. Moreover, we investigated the quandum oscillations of Cd_3As_2.

Keywords: large hall angle, two-band transport model, Cd_3As_2 material, quantum oscillations

Contents

Chapter 1 Introduction

1.1 Background

As the improvement of integarated cirucit industry, we have stepped into the post-Moore age, which means devices that manufactured by traditional fabrication process cannot conform to the need of Moore's law's forecast as the properties of materials will change as the quantum effect is enlarged. The industry gives some solutions that may solve this problem, one of them is using new kind of semiconductor materials to manufacture electronic devices. Since the carrier mobility of materials will degrade as the device is narrowed in a small size, finding materials with high mobility is necessary. The reasons that materials have high mobility is mostly because of their special lattice structures and band structures, so what we care about is how to measure material's physical parameters such as carrier mobility or carrier density more exactly and give an analysis of the material. For traditional semiconductor materials, the measuring method is consummate, however, for high mobility materials, charges are transported in high magnetic field and large hall angle situation, which means we cannot apply traditional method in this case. This paper gives a generic method to analyze materials which works in high field and large hall angle by combining theorerical analysis and experimental data.

1.2 Method for Measurement

In electric transportation, what we care about are parameters like carrier density, carrier mobility and conductivity of the material. Carrier density describes the number of two kinds of carriers (electrons or holes) in the material. Carrier mobility shows how fast that this kind of carrier can move in the material, in general, the value of it is the average velocity of the carrier in a unit electric field. Conductivity has a direct relationship with the resistance of the material and it is related to the temperature.The value of conductivity is associated with carrier density and mobility, that is $\sigma = nq\mu_n + pq\mu_p$, so acquiring the value of carreir density and mobility is one of the key processes in investigating the electric properties of a kind of material. This part will give some frequently-used methods for grabbing these parameters.

1.2.1 Method of Measuring Carrier Density

Carrier density is an important parameter of semiconductor materials since the manufacturer can optimize the performance of devices by regulate and control the

carrier density. For new materials, carrier density is also a key parameter to determine the conductivity. In reality, there are many methods to measure the carrier density of materials. In this part, the SdH Oscillation method is showed there.

SdH oscillation occurs at sufficiently low temperature in the presence of large magnetic field. This effect was first observed by A.B.Fowler and his fellows in 1966 when they were applying hall measurement to a NPN MOSFET. They observed the oscillation of conductance to the gate voltage as shown in Figure 1.1. [6]

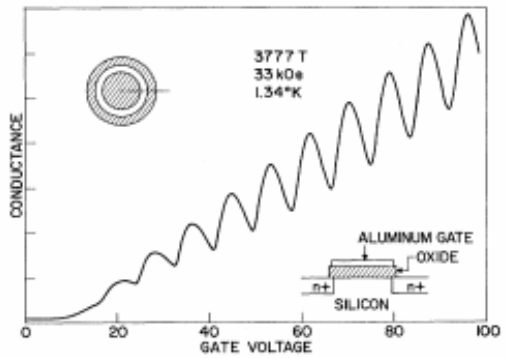

Figure 1.1: The conductance as a function of gate voltage at a magnetic field as 33kOe. In the lower right-band corner, a section through the structure is shown.

The frequency of SdH oscillation sigal has a relationship with the carrier density as below:

$$f = \frac{1}{\Delta\frac{1}{B}} = \frac{1}{\frac{1}{B_{n+1}} - \frac{1}{B_n}} = \frac{\hbar k_F^2}{2e} = \frac{n_{2D}h}{2e} \tag{1.1}$$

In Eq (1.1), n_{2D} is the carrier density of two-dimentional electron gas. From the equation, it is clear that SdH oscillation method has the advantage of simplicity and clarity. However, since SdH oscillation only can be observed at sufficiently low temperature and large magnetic field, this method cannot be used in measuring traditional semiconductor materials with low carrier mobility.

1.2.2 Method of Measuring Carrier Mobility

Carrier mobility shows how fast that this kind of carrier can move in the material, its value is equal to the drift velocity under the unit electric field as $\mu = \frac{\bar{v}}{E}$. In the equation, μ is the carrier mobility, $\bar{v}$ is the average velocity of carrier in the material and E is the electric field. Ideally, carriers can be accelerated in the electric field until it reach the light velocity, however, because of the scattering, carriers will reach a steady velocity, which is related to the mean free time τ, the average time between two scattering of the carrier. Therefore, the mobility can be expressed as: $\mu_n = \frac{q\tau_n}{m_n^*}$ and $\mu_p = \frac{q\tau_p}{m_p^*}$. In reality, there are many methods to measure the carrier mobility of materials. In this part, the $I-V$ method is showed there.

$I-V$ method is used for measuring the carrier mobility for semiconductor devices. For example, the $I-V$ characteristic curve of a long-channel n-type MOSFET is shown below. A p-type one is quite similar.

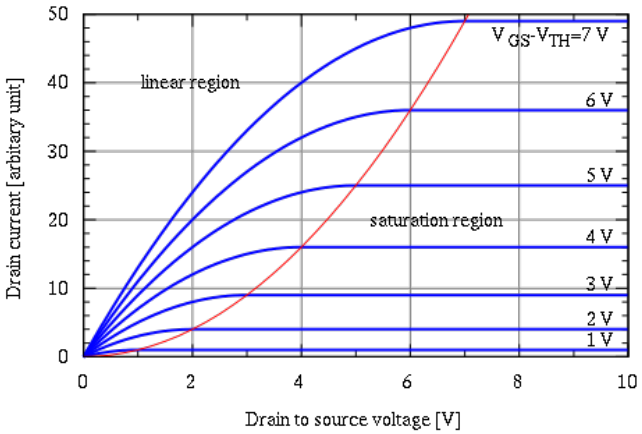

Figure 1.2: MOSFET drain current versus drain-to-source voltage for several values of $V_{GS} - V_{th}$; the boundary between linear and saturation region is indicated by an upward parabola curve.

It has two parts, one is linear region and the other one is the saturation region. In linear region, the $I - V$ relation can be expressed as

$$I_D = \frac{W\mu_n C_{ox}}{2L}[2(V_{GS} - V_{th})V_{DS} - V_{DS}^2]^{[19]} \tag{1.2}$$

And for saturation region, it is

$$I_D = \frac{W\mu_n C_{ox}}{2L}(V_{GS} - V_{th})^{2\,[19]} \tag{1.3}$$

In Eq (1.2) and Eq (1.3), L and W is the length and the width of the device, C_{ox} is the capacitance of oxide layer. By measuring the $I - V$ characteristic curve of the device, one can easily get the value of μ_n. For a p-type device, we can calculate the value of μ_p. However, this is the carrier mobility in the conduction channel, which is different from the intrinsic carrier mobility of the material, in other word, it's not the value we want to get but a parameter in simulating a device. Taking this weakness into account, this method is only suitable for measuring the channel carrier mobility of a device but not the value of carrier mobility of a material.

1.2.3 Method of Measuring Conductivity

Conductivity demonstrates the ability that the material can conduct electricity. A large conductivity means the material can conduct electricity easily. There are many methods to measure the carrier mobility and conductivity. This part will give a general introduction of three of them, Four Probe Method, Van der Pauw Method and Hall Effect Method.

1.2.3.1 Four Probe Method

Four probe method is commonly used in measuring the conductivity of a material. The connection setting that how this method works is shown in Figure (1.3).

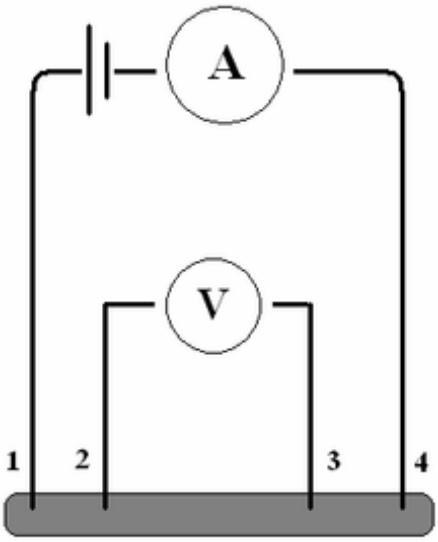

Figure 1.3: Four-probe method setting: Measuring the voltage between terminal 2 and 3 and current is supplied between terminal 1 and 4.

Placing four probes on the surface of the material, giving a current I between terminal 1 and 4 and measure the voltage V between the other two, then the value of conductivity is:

$$g = \frac{I}{2\pi V S} \tag{1.4}$$

In Eq (1.4), S is the distance between two probe. This method is quick and simple but its weakness is that the accuracy of the result is not satisfied, so this method is usually used in industry other than in laboratory.

1.2.3.2 Van der Pauw Method

Van der Pauw method is first proposed by Van der Pauw in 1958[21], it's a technique used to measure the resistivity(the reciprocal of conductivity) and hall coefficient of a sample. It can be applied to any sample as long as it's approximately two-dimensional, solid and electrodes are placed around the edge. Although one can take any points on the edge, it is better for the accuracy of result if it fits the condition that AB is perpendicular to CD.

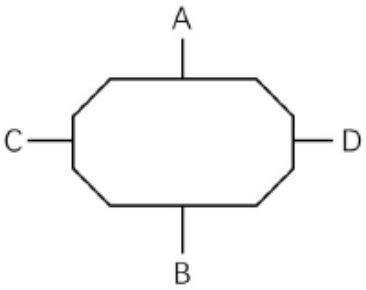

Figure 1.4: Van der Pauw method setting: Measuring the voltage between terminal D and B and current is supplied between terminal A and C. Similarly, measuring the voltage between terminal C and B and current is supplied between terminal A and D.

Figure (1.4) shows how to apply the Van der Pauw method to the sample. Supply a current I_{AC}between terminal A and C, then measure the voltage V_{DB}, take the value of R_1 as $R_1 = \frac{V_{DB}}{I_{AC}}$. Similarly, one can get the value of R_2 as $R_2 = \frac{V_{CB}}{I_{AD}}$. From Van der Pauw's equation:

$$\rho = \frac{\pi d}{ln2} \frac{R_1 + R_2}{2} f(\frac{R_1}{R_2}) \tag{1.5}$$

In Eq (1.5), d is the thickness of the sample, $f(x)$ is the Van der Pauw correction function. The weak point of Van der Pauw method is that it can only be used in a uniform sample.

1.2.3.3 Hall Effect Method

Hall effect method is a general method that can be used to get the value of carrier density, carrier mobility and conductivity of the material. Hall effect was discovered by Edwin Hall in 1879.[8]

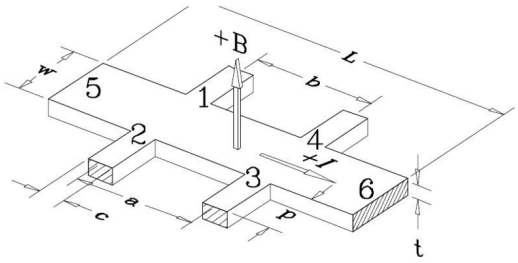

Figure 1.5: A current is supplied from terminal 5 to terminal 6. A magnetic field B is applied which is perpendicular to the surface of the example. The voltages between terminal 1, 2, 3 and 4 are measured.

Figure (1.5) shows the general appearance of a hall bar. A current is supplied from terminal 5 to terminal 6. A magnetic field B is applied which is perpendicular to the surface of the example. The voltages between terminal 1, 2, 3 and 4 are measured.

The hall effect can be concluded as when charges are subjected to an external perpendicular magnetic field, the Lorentz force would deflect the electrons away from their original conduction direction, hence giving rise to a non-zero transverse electric field.

Taking a hole as an example, the mechanical equation can be expressed as

$$E_y q = q v_x B_z \text{ [19]} \tag{1.6}$$

$$J_x = pqv_x \tag{1.7}$$

Combine Eq (1.6) and Eq (1.7), we can conclude that

$$p = \frac{J_x B_z}{E_y q} \tag{1.8}$$

In Eq (1.8), E_y, B_z and J_x are all known values, therefore the carrier density can be calculated.

We can measure the voltage difference along the current direction and perpendicular to current direction, say V_{14} and V_{12}. Assume there is no velocity saturation, then it has the relation that $v_x = \mu E_x$, and in equilibrium, $E_y = v_x B_z$. Then we can get the expression of μ, that is $\mu = \frac{E_y}{E_x B_z}$. Further more, we can conclude that

$$\mu = \frac{V_{12} L}{V_{14} W B_z} \tag{1.9}$$

where L and W are the length and width of the example.

Since the hall effect method can be used to measure both the carrier density and mobility, we will apply this method in the measurement.

1.3 Classical Model in Carrier Transportation

According to the classical hall effect theory, the Hall angle θ_H, which is defined as the angle between induced electric field and the current, and its tangent value is $tan(\theta_H) = \mu B$[17], where μ is the carrier mobility and B is the applied magnetic field. In most cases, since the carrier mobility is not too much large, the tangent value of the hall angle should be less than 1. For example, the carrier mobility of silicon is $1350 cm^2/v{\cdot}s$, then under a magnetic field as $3T$, the value of $tan\theta_H$ is 0.405, which is far less than 1. However, for material with large carrier mobility, this model is not suitable since the value $tan\theta_H$ cannot guarantee this condition. A new model that can be used for analyzing the material in large hall angle condition is necessary. This paper exhibits a general model that can analyze all the materials no matter how large its carrier mobility is and what kind of condition it's working in.

Chapter 2 Experimental Instrments of Measuring Cd_3As_2

Figure (2.1) shows the general connection graph of measuring a sample. The sample is placed in the Oxford system. Model 6221 sypplies the current across the sample and SR830s will measure the voltage signal V_{xx} and V_{xy}.

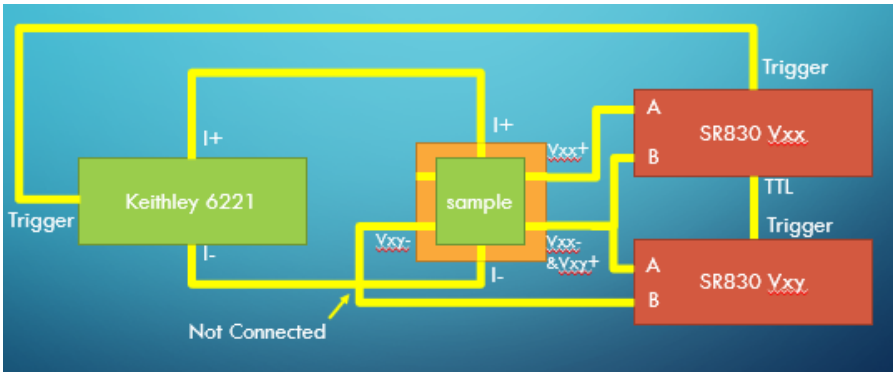

Figure 2.1: General connection graph of measuring a sample

2.1 Introduction of Sample

Cadmium arsenide (Cd_3As_2) is an inorganic semimetal in the II-V family. In 2014, Cd_3As_2 was shown to be a semimetal material analogous to graphene that exists in a 3D form that should be much easier to shape into electronic devices. What's more, Cd_3As_2 shows a degenerate n-type semiconductor intrinsic conductivity with a large carrier mobility.[13,14,22] These advantages make Cd_3As_2 more attractive and now Cd_3As_2 has become one of today's hottest materials. The sample is cut as the shape of a hall bar like Figure (1.5)and bonded on a support like Figure (2.2).

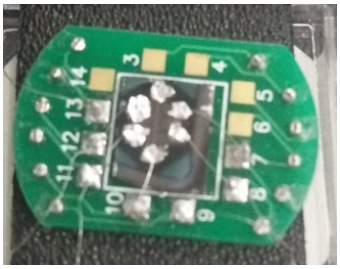

Figure 2.2: Hall bar of Cd_3As_2

2.2 Introduction of Hardwares

2.2.1 Model SR830 DSP Lock-In Amplifier

SR830 is a DSP lock-in amplifier. Lock-in amplifiers are used to detect and measure very small AC signals. The amplitude of measurement ranges from 1e-6 volts to 1 volts. Too small or too large signal cannot be detected.

Figure 2.3: Front panel of SR830

Lock-in amplifiers use a technique known as phase-sensitive detection to single out the component of the signal at a specific reference frequency. It works like a band-pass filter with a narrow band and a high quality factor.

In the diagram below, the reference signal is a square wave at frequency ω_r, which might be the sync signal from a function generator. Correspondingly, the sine output from the function generator will be shown as in the picture. To extract the input signal, SR830 will generate its own lock-in signal as a reference signal.

The input signal and the lock-in signal can be described as follow:

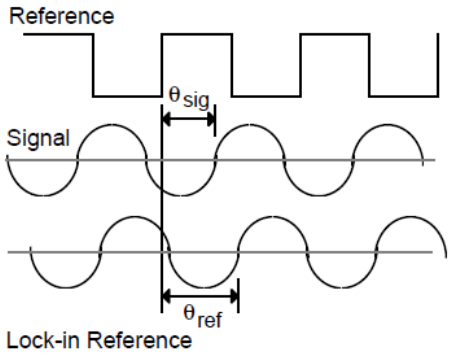

Figure 2.4: Principle of locking the frequency

$$\begin{cases} V_{input} & = V_{sig}\sin\left(\omega_r t + \theta_{sig}\right) \\ V_{lock-in} & = V_L \sin\left(\omega_L t + \theta_{ref}\right) \end{cases} \tag{2.1}$$

What SR830 does is multiply the two signals and pass the output through a low pass filter. The mathematic process is shown below

$$\begin{aligned} V_{psd} &= V_{sig}V_L \sin\left(\omega_r t + \theta_{sig}\right)\sin\left(\omega_L t + \theta_{ref}\right) \\ &= \frac{1}{2}V_{sig}V_L \cos\left[(\omega_r - \omega_L)t + \theta_{sig} - \theta_{ref}\right] \\ &- \frac{1}{2}V_{sig}V_L \cos\left[(\omega_r + \omega_L)t + \theta_{sig} + \theta_{ref}\right] \end{aligned} \tag{2.3}$$

After the low pass filter,

$$\begin{aligned} V_{psd} &= \frac{1}{2} V_{sig} V_L \cos\left[(\omega_r - \omega_L)t + \theta_{sig} - \theta_{ref}\right] \\ &= \frac{1}{2} V_{sig} V_L \cos\left(\theta_{sig} - \theta_{ref}\right) \end{aligned} \tag{2.5}$$

When the frequency of lock-in signal is the same with the frequency of input signal, the output of the system should be a dc signal, in other word, it has been locked.

2.2.2 Model 6221 AC and DC Current Source

The Model 6221 AC and DC Current Source combines ease of use with low current noise. Low current sourcing is important to applications in the semiconductor industries. High sourcing accuracy and built-in control functions makes the Models 6221 ideal for applications like Hall measurements, and accurate resistance measurements.

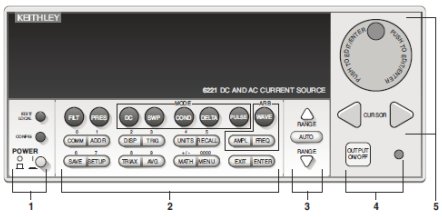

Figure 2.5: Front panel of Model 6221

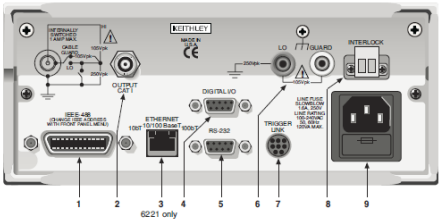

Figure 2.6: Rear panel of Model 6221

2.2.3 Oxford Integrated Cryogen Free Superconducting Magnet System with Variable Temperature

The key part of controlling the precision measurement system is the control of temperature and magnetic field. Cryogen free superconducting magnet system providing top loading access to a sample in a variable magnetic field and low temperature environment. The low temperature environment is accomplished by Io, which offers device temperature down to 50mK with a Heliox VT ^{3}He refrigerator.

Figure 2.7: Oxford system

Oxford system could offer these advantages.

- Standard magnetic fields up to 14 T in a compact geometry
- Vector rotate magnet geometries available
- No cryogens needed, just electricity supply
- Uses the highest specification superconducting wire available on the market
- Lowest vibration: suitable for a wide range of sensitive measurements

The Mercury range includes a MercuryiTC temperature controller, a MercuryiPS-M master magnet power supply and a MercuryiPS-S slave magnet power supply.

Figure 2.8: Mercury iTC

Figure 2.9: Mercury iPS

The Mercury iTC temperature controller is ideally suited to monitor and control the Optistat Dry. It has one PID loop to read the sensor and control the heater mounted on the cryostat. The MercuryiPS enables automated control of a wide range of superconducting magnets, including NMR, high field, beamline and Vector Rotate magnet systems.

2.3 Introduction of Software

We use LabVIEW to control the system. All instruments are conncected to the PC by a GPIB line. Laboratory Virtual Instrument Engineering Workbench (LabVIEW) is a system-design platform and development environment for a visual programming language from National Instruments.

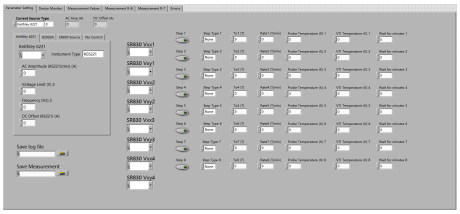

Figure 2.10: Parameters setting

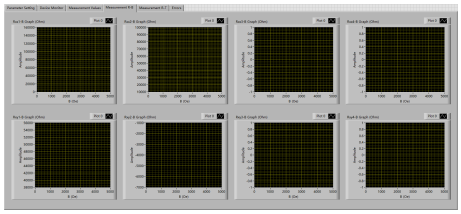

Figure 2.11: Measurement result

Figure (2.10) and Figure (2.11) are the parameters setting interface and measurement results interface of the software. User can choose what kind of process the system will implement (sweep field or sweep temperature). Moreover, the software can give a preliminary analysis of the measurements and show the result in real time. Data will be saved in the created txt file. The logfile will record the state of system like gasflow, VTI temperature and so on. The measurement file will record the measurement result like R_{xx}, R_{xy} of all the SR830s.

Chapter 3 LabVIEW Software Design

This part shows the design thought of every module and each subprogram flow in detail. In the first part, it will give the modules used in the program. And in the second and third part, a general picture of how the program works will also be given.

3.1 Modules for Controlling Oxford System

In this part, each module in the system is introduced in detail there, including the reading modules and controlling modules.

3.1.1 Read States of System

In previous part, the Oxford system is controlled by the Mercury system, so to read out the states of the system, we need to connect the PC to the Mercury system with network lines. As the IP address are set, we can read the data as below.

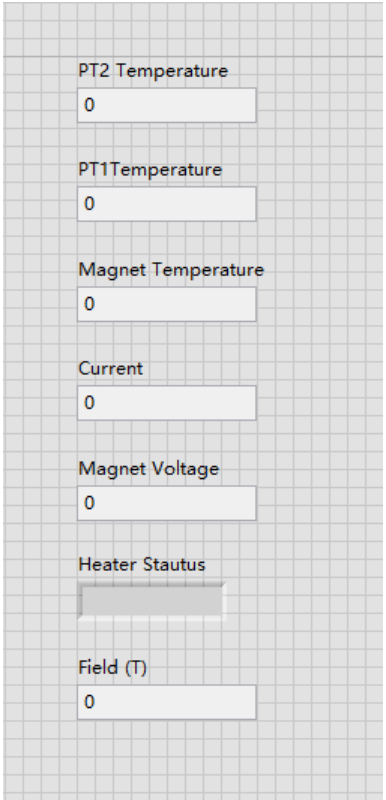

Figure 3.1: Read the magnetic field and temperature of magnet.

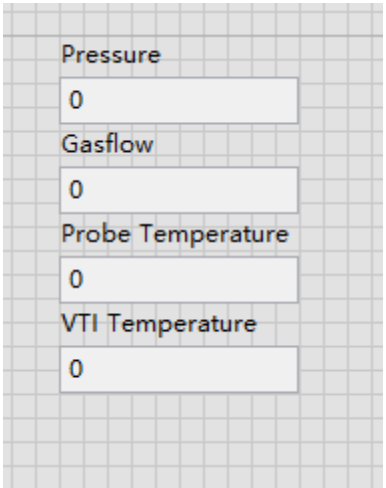

Figure 3.2: Read the temperature of the system

In Fig (3.1), there shows the temperature of PT1, PT2 and magnet temperature, the current, voltage and magnetic field of the magnet, the heater status is also showed there. PT1 is the first-stage freezer, in most cases, its temperature is around 50K. PT2 is the second-stage freezer, and its temperature is around 3.5K. To give a detailed explanation of magnet temperature, the mechanism of how the magnet engender the field should be given.

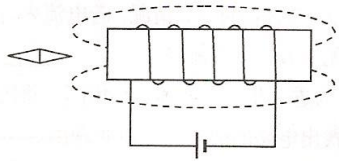

Figure 3.3: Electrical magnet

As shown in Fig (3.3), the magnet is wraped up by the wires. When a current is applied to the magnet, a strong magnetic field will be engendered along the longitudinal direction. The value of current applied is proportional to the magnetic field engendered as $B = A{\cdot}I$. The current and the magnetic field mentioned here are also shown in the module. However, to keep the stability of the system, the current cannot be applied abruptly, or the system will go quench. The extent that the system is close to quench is characterized as the magnet temperature. In most cases, the magnet temperature is around 3.3K, and when its value is over 4K, the system is close to quench. The heater is used to control the magnetic field, only when the heater status is on that the magnetic field can be adjusted.

In Fig (3.2), it shows the temperature of probe and VTI, pressure and gasflow. The probe temperature is equal to the environment that the sample is placed in, the VTI is the shield of probe, in most cases, VTI temperature is near the probe temperature. The pressure will effect the velocity of cooling of the probe, and the gasflow will effect the pressure.

By reading these parameters, one can keep abreast of the system and decide what command to adjust the system.

3.1.2 Controllment of Cooling System

In most cases, we apply hall measurement to the sample under different magnetic fields and temperatures, so controlling the magnetic field and temperature are the most important and frequently used part of the controlling modules.

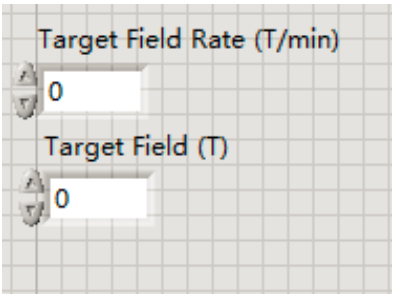

Figure 3.4: Front panel of setting magnetic field

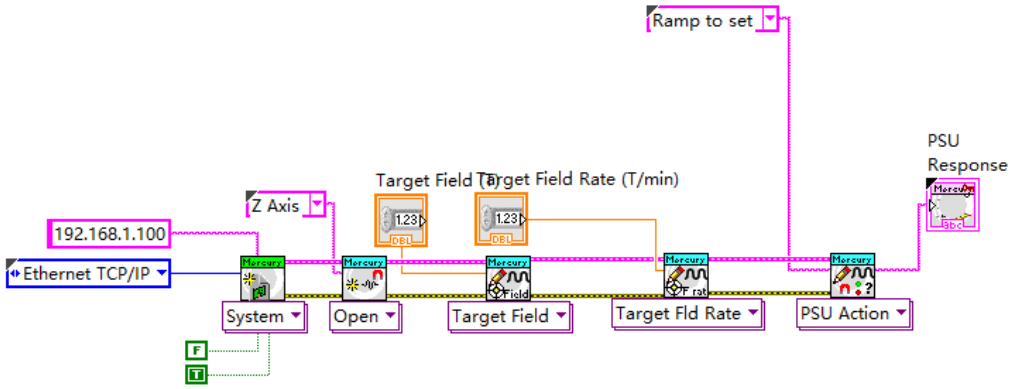

Figure 3.5: Block Diagram of setting magnetic field

Fig (3.4) and (3.5) show the front panel and block diagram of the setting magnetic field module. The user can set the target field and the velocity to reach the target field. In case of the high temperature of the magnet, the field rate should be set below 0.1.

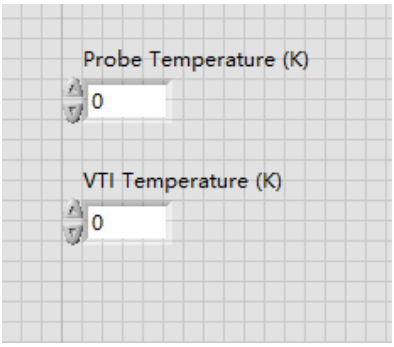

Figure 3.6: Front panel of setting probe and VTI temperature

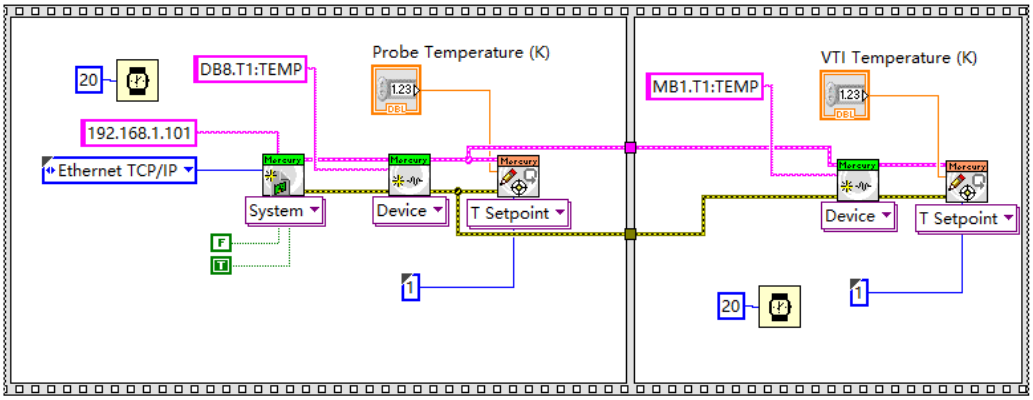

Figure 3.7: Block Diagram of setting probe and VTI temperature

Fig (3.6) and (3.7) show the front panel and block diagram of the setting temperature module. The user can set the probe and VTI temperature. The value of

VTI temperature should be close to the probe temperature. The rate of cooling is set automatically by the system.

3.1.3 Read Resistance & Voltage by SR830

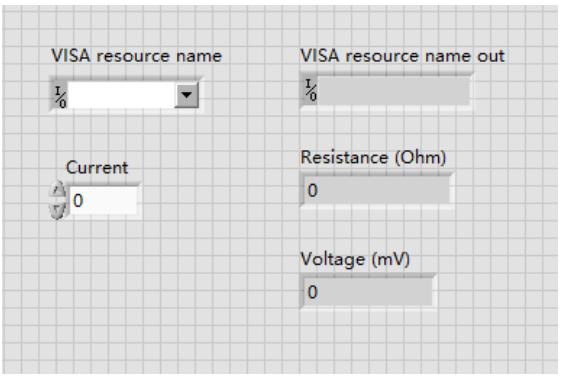

Figure 3.8: Front panel of reading resistance by SR830

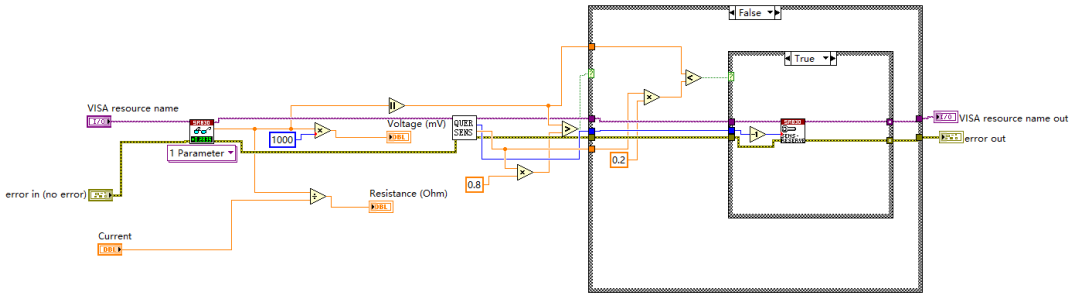

Figure 3.9: Block Diagram of reading resistance by SR830

Fig (3.8) and (3.9) show the front panel and block diagram of the reading SR830 module. User can get the resistance and the voltage across the sample. In Fig (3.8), the VISA input is the address of the instrument since there are more than 10 instrments that will be used at the same time. To identify them apart, each one will have a unique address, and the VISA input is for filling in this address. The input current is for calculating the resistance of the sample since SR830 can only measure the voltage across the sample. In Fig (3.9), the left part is for reading and calculating the resistance and for the right part, it is for adjusting the sensitivity of the instrment automatically. For lower sensitivity, the measurement will be more accurate. When the value of measurement is beyond the 80% of the full range or below the 20% of the full range, the sensitivity will be adjusted to a higher or a lower level properly.

3.1.4 Setting Current by Model 6221

Fig (3.10) and (3.11) show the front panel and block diagram of the setting Model 6221 module. User can set the AC amplitude, wave frequency and DC offset of the current applied to the sample. In Fig (3.10), the function of VISA input is the same

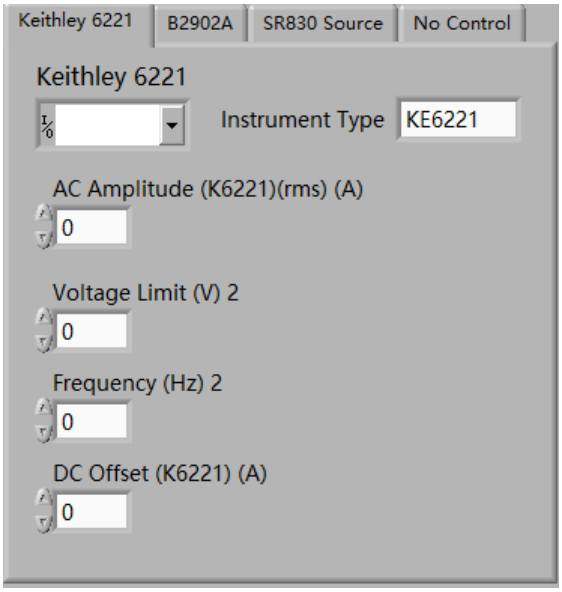

Figure 3.10: Front panel of setting current by Model 6221

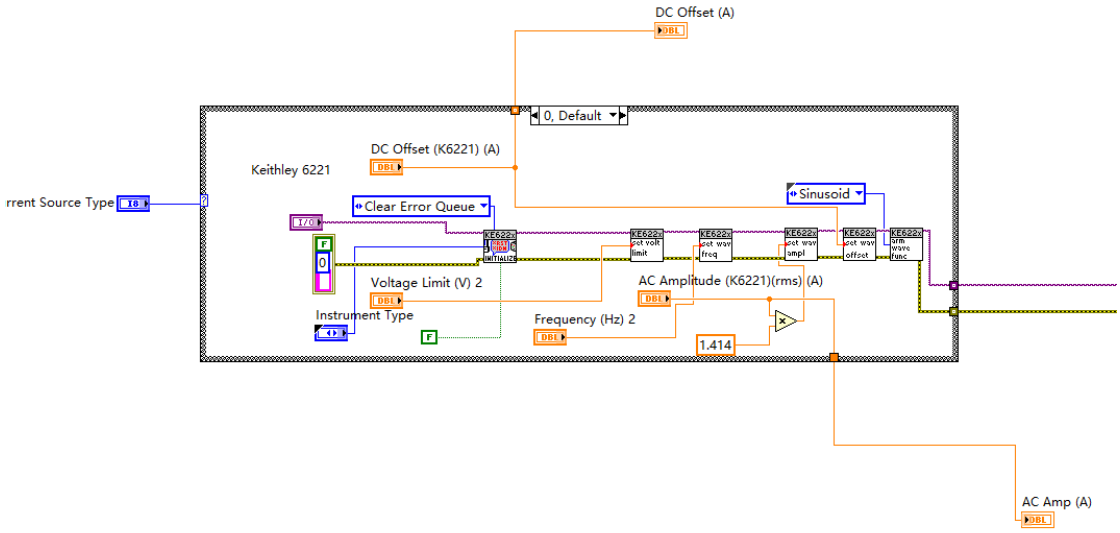

Figure 3.11: Block Diagram of setting current by Model 6221

with which in SR830 module, that is for filling in the GPIB address. The AC amplitude, frequency and DC offset are parameters that can determine the input signal. Voltage limit is for protecting the circuit from being destroyed since a large current will release heat greatly which may damage the circuit.

3.1.5 Saving Data

Fig (3.12) shows the saving data menu in the front panel. In this program, data is divided into two categories, log data and measurement data. Log data include the states of the system like PT1, PT2 temperatures, while the measurement data include the resistance and voltage that SR830s get. Data will be saved as long as one step is completed.

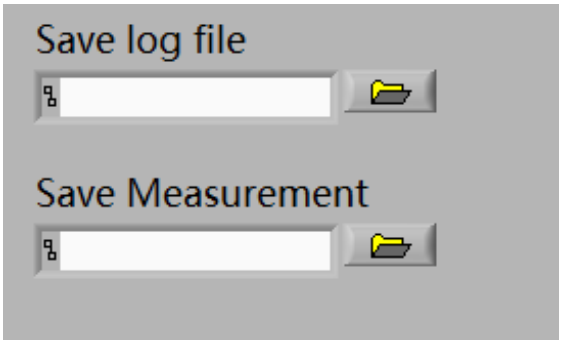

Figure 3.12: Front panel of saving data

3.2 Operation Principle

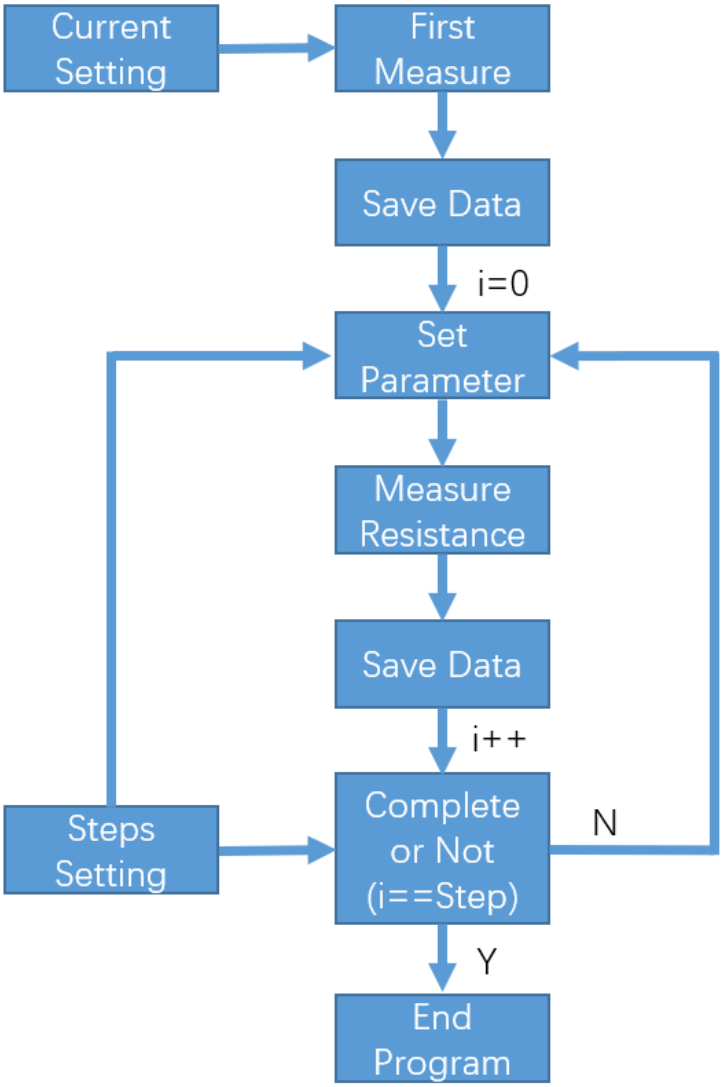

Figure 3.13: Flowchart of the program

The flowchart of the program is shown in Fig (3.13). Firstly, user need to set the current input and step loops. Current input has been explained in previous part, step loops will be explained in detail here.

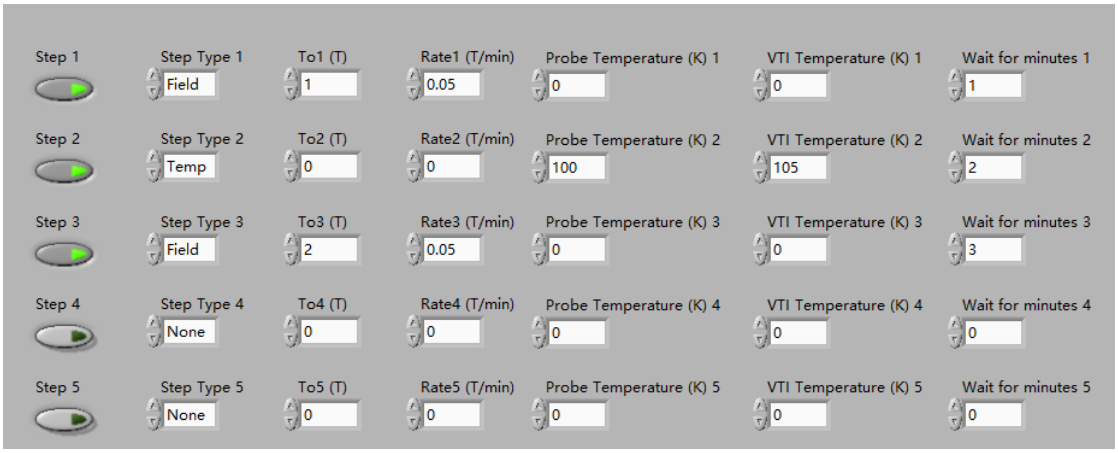

Figure 3.14: Step loops input

Fig (3.14) shows the step loops information. One step can either be sweeping the magnetic field or sweeping the probe temperature. In this case, three steps will be operated since three buttons are pressed down. The first step is setting the magnetic field to 1T with the rate as 0.05T/min, then wait for 1 minutes to cool down the magnet, second one is setting the probe and VTI temperatures as 100K and 105K and then wait for 2 minutes, third one is also setting the magnetic field to 2T with the rate as 0.05T/min and wait for 3 minutes.

After setting the current input and step loops, the system will start its first measurement, which is for testing whether the system can work. The testing data will also be saved. After this, like a "for" loop, a counter will be initialized, and each loop will follow the process of seting parameters, measuring resistance, saving data and deciding whether to end the loop. After the "for" loop process is finished, the program will also be terminated.

3.3 Measurement & Data Saving

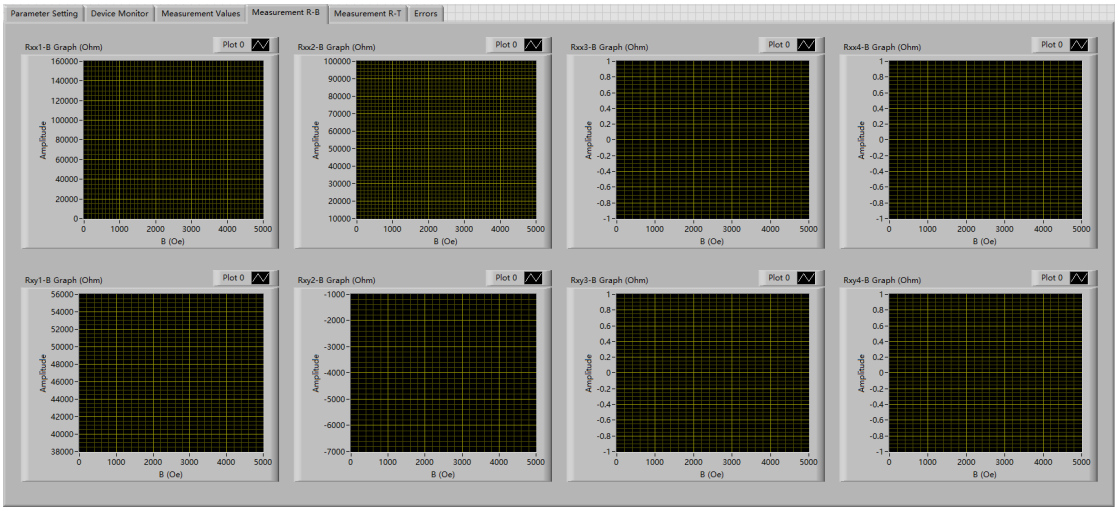

Figure 3.15: Measured resistance R versus magnetic field B

Fig (3.15) shows the resistance versus magnetic field figure when the program is

working. It can show the trend of the resistance in real time.

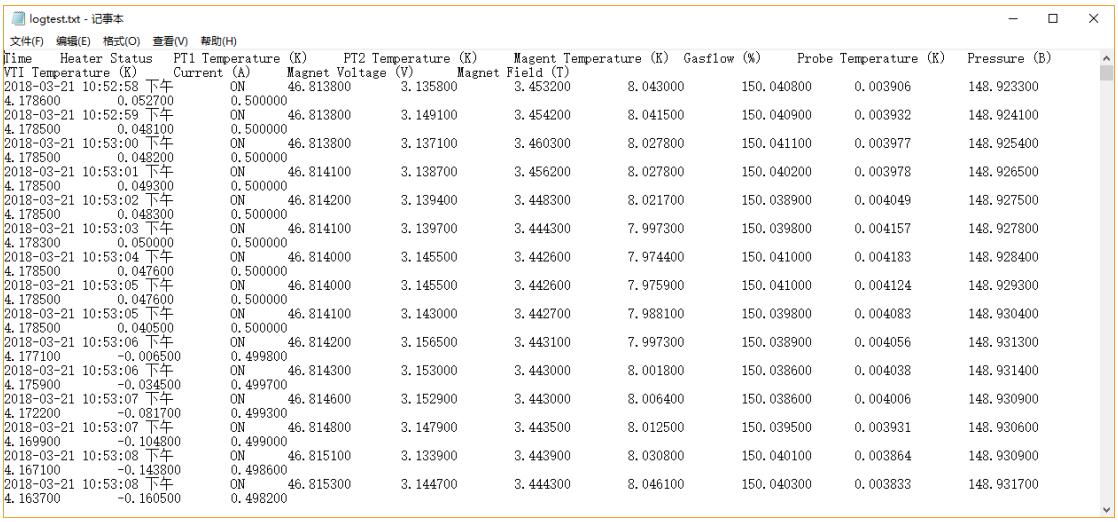

logtest.txt - 记事本

文件(F) 编辑(E) 格式(O) 查看(V) 帮助(H)

Time	Heater Status	PT1 Temperature (K)	PT2 Temperature (K)	Magent Temperature (K)	Gasflow (%)	Probe Temperature (K)	Pressure (B)
VTI Temperature (K)	Current (A)	Magnet Voltage (V)	Magnet Field (T)				
2018-03-21 10:52:58 下午	ON	46.813800	3.135800	3.453200	8.043000	150.040800	0.003906	148.923300
4.178600	0.052700	0.500000					
2018-03-21 10:52:59 下午	ON	46.813800	3.149100	3.454200	8.041500	150.040900	0.003932	148.924100
4.178500	0.048100	0.500000					
2018-03-21 10:53:00 下午	ON	46.813800	3.137100	3.460300	8.027800	150.041100	0.003977	148.925400
4.178500	0.048200	0.500000					
2018-03-21 10:53:01 下午	ON	46.814100	3.138700	3.456200	8.027800	150.040200	0.003978	148.926500
4.178500	0.049300	0.500000					
2018-03-21 10:53:02 下午	ON	46.814200	3.139400	3.448300	8.021700	150.038900	0.004049	148.927500
4.178500	0.048300	0.500000					
2018-03-21 10:53:03 下午	ON	46.814100	3.139700	3.444300	7.997300	150.039800	0.004157	148.927800
4.178300	0.050000	0.500000					
2018-03-21 10:53:04 下午	ON	46.814000	3.145500	3.442600	7.974400	150.041000	0.004183	148.928400
4.178500	0.047600	0.500000					
2018-03-21 10:53:05 下午	ON	46.814000	3.145500	3.442600	7.975900	150.041000	0.004124	148.929300
4.178500	0.047600	0.500000					
2018-03-21 10:53:05 下午	ON	46.814100	3.143000	3.442700	7.988100	150.039800	0.004083	148.930400
4.178500	0.040500	0.500000					
2018-03-21 10:53:06 下午	ON	46.814200	3.156500	3.443100	7.997300	150.038900	0.004056	148.931300
4.177100	-0.006500	0.499800					
2018-03-21 10:53:06 下午	ON	46.814300	3.153000	3.443000	8.001800	150.038600	0.004038	148.931400
4.175900	-0.034500	0.499700					
2018-03-21 10:53:07 下午	ON	46.814600	3.152900	3.443000	8.006400	150.038600	0.004006	148.930900
4.172200	-0.081700	0.499300					
2018-03-21 10:53:07 下午	ON	46.814800	3.147900	3.443500	8.012500	150.039500	0.003931	148.930600
4.169900	-0.104800	0.499000					
2018-03-21 10:53:08 下午	ON	46.815100	3.133900	3.443900	8.030800	150.040100	0.003864	148.930900
4.167100	-0.143800	0.498600					
2018-03-21 10:53:08 下午	ON	46.815300	3.144700	3.444300	8.046100	150.040300	0.003833	148.931700
4.163700	-0.160500	0.498200					

Figure 3.16: Log file in txt format

measuretest.txt - 记事本

文件(F) 编辑(E) 格式(O) 查看(V) 帮助(H)

The AC amp is 0.000001(A). The DC Offset is 0.000000(A).

Magnet Field (Oe)	Vxx(mV)	Vxy(mV)
5000.000000	0.000000	3.604430
5000.000000	0.000000	3.604430
5000.000000	0.000000	3.604430
4998.000000	0.000000	3.604430
4997.000000	0.000000	3.604430
4993.000000	0.000000	3.604430
4990.000000	0.000000	3.604430
4986.000000	0.000000	3.604430
4982.000000	0.000000	3.604430
4980.000000	0.000000	3.604430
4973.000000	0.000000	3.604430
4970.000000	0.000000	3.604430
4963.000000	0.000000	3.604430
4956.000000	0.000000	3.604430
4951.000000	0.000000	3.604430
4947.000000	0.000000	3.604430
4939.000000	0.000000	3.604430
4935.000000	0.000000	3.604430
4929.000000	0.000000	3.604430
4922.000000	0.000000	3.604430
4918.000000	0.000000	3.604430
4909.000000	0.000000	3.604430
4904.000000	0.000000	3.604430
4895.000000	0.000000	3.604430
4885.000000	0.000000	3.604430
4881.000000	0.000000	3.604430
4871.000000	0.000000	3.604430
4865.000000	0.000000	3.604430
4861.000000	0.000000	3.604430
4851.000000	0.000000	3.604430

Figure 3.17: Measurement file in txt format

Fig (3.16) and Fig (3.17) show the log file and measurement file saved in the txt format. All the data can be easily copied and taken into other analysis software directly.

3.4 Summary

In this section, a general introduction of the program is given, including the modules used in the program, the operate principle and the results. Users may modify the program as their own need.

Chapter 4 Carrier Transportation Model in Constant EM Fields

4.1 Carrier Transportation in Semiconductors

To study how carriers are moving in the material, we need to know how electrons are existing in the material. According to Bloch Theorem[11], because of the periodicity of the lattice, electrons' states should follow the Schrodinger's equations[16], that is

$$[-\frac{\hbar^2}{2m_0}\nabla^2 + V(r)]\psi = E\psi \tag{4.1}$$

Then we can get the state of electrons, which is the general solution of Eq (4.1). However, in more general cases, there are not only periodic potential field in the lattice but also external field like electric and magnetic fields. What's more, because of the defects in the material, the periodicity of the lattice is broken, scattering will happen and affect the transportation of carriers. In general, there are external fields and scattering will also have an effect on the moving of carriers. If the scattering type is determined, we can propose a new model of carrier transportation and decide what parameters we should use to determine the state of the carriers.

4.2 Hall Effect Model

4.2.1 Hall Effect with Single Carrier Model

The electron based hall effect is shown in Fig (4.1).

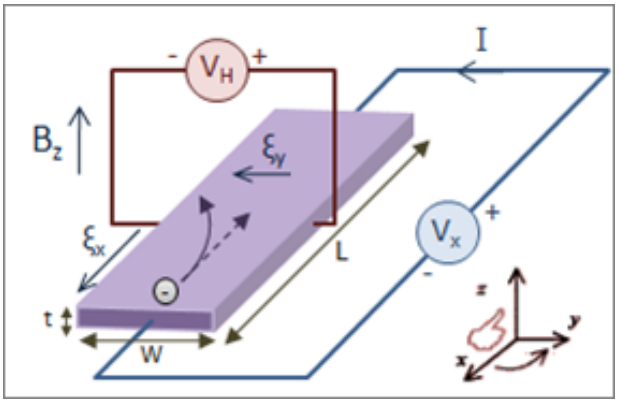

Figure 4.1: Hall effect of electrons

For an electrified n-type semiconductor, the external current direction is along positive x-axis, then the velocity of electrons are along negative x-axis. The direction of magnetic field B_z is along positive z-axis. Because of the Lorenz force, electrons will have a velocity along negative y-axis, and to equalize the force in y direction, an electric field along negative y-axis will be induced. Because of the existance of E_y, the original electric field is deflected and the the angle between them is defined as hall angle. For n-type semiconductors, the value of hall angle θ_n is negative and correspondingly, for p-type semiconductors, it's positive.

In hall effect, E_y is proportional to the current density J_x and magnetic field B_z, that is

$$E_y = R_H J_x B_z \tag{4.2}$$

With Eq (1.7), we have

$$R_H = \frac{E_y}{J_x B_z} = -\frac{1}{nq} < 0 \tag{4.3}$$

Similarly, we can get some conclusions for holes.

$$R_H = \frac{E_y}{J_x B_z} = \frac{1}{pq} > 0 \tag{4.4}$$

To ensure Eq (4.3) and Eq (4.4) work, there are three prerequisites.

- There is only one kind of carriers, either electrons or holes.
- Hall angle is small enough so that $tan(\theta_H) < 1$.
- Mean free time of carriers are equivalent.

4.2.2 Hall Effect with Two Carriers Model

For semiconductor materials with high mobility, there can be two kinds of carriers that are taking part in conducting electricity. Then first prerequisite in the above part is not needed anymore. In equilibrium, the hall current for electrons and holes cancels with each other, then the totoal current along y-axis is zero.

For holes, the the drift current caused by the electric field along positive y-axis is

$$J_{hole,E} = pq\mu_p E_y \tag{4.5}$$

And the current along negative y-axis caused by Lorenz force is

$$J_{hole,B} = -pq\mu_p \frac{qv_{p,x}B_z}{q} = -pq\mu_p v_{p,x} B_z = -pq\mu_p^2 E_x B_z \tag{4.6}$$

Similarly, for electrons, we have

$$J_{electron,E} = nq\mu_n E_y \tag{4.7}$$

$$J_{electron,B} = nq\mu_n \frac{qv_{n,x}B_z}{q} = nq\mu_n v_{n,x} B_z = nq\mu_n^2 E_x B_z \tag{4.8}$$

Because the total current is zero, we have

$$\begin{aligned} J_{total} &= J_{hole,E} + J_{hole,B} + J_{electron,E} + J_{electron,B} \\ &= pq\mu_p E_y - pq\mu_p^2 E_x B_z + nq\mu_n E_y + nq\mu_n^2 E_x B_z = 0 \end{aligned} \tag{4.10}$$

Then we have the expression of E_y

$$E_y = \frac{p\mu_p^2 - n\mu_n^2}{(p\mu_p + n\mu_n)} E_x B_z \tag{4.11}$$

Substitute E_x with $E_x = \frac{J_x}{q(p\mu_p + n\mu_n)}$, Eq (4.11) becomes

$$E_y = \frac{1}{q} \frac{p\mu_p^2 - n\mu_n^2}{(p\mu_p + n\mu_n)^2} J_x B_z \tag{4.12}$$

According to the definition of hall coefficient, $R_H = \frac{E_y}{J_x B_z}$, it can be expressed as

$$R_H = \frac{1}{q} \frac{p\mu_p^2 - n\mu_n^2}{(p\mu_p + n\mu_n)^2} \tag{4.13}$$

Eq (4.13) is the new expression of hall coefficient in two carriers model under small hall angle. When p is equal to zero, which means there is only one kind of carrier, electrons, then the equation can be refined as $R_H = -\frac{1}{nq}$, which is the same with Eq (4.3). Similarly, this equation is suitable for situation that there are only holes, so this model is suitable for both single carrier and two carriers model. In intrinsic case, which has $n = p = n_i$, Eq (4.13) becomes

$$R_H = \frac{1}{n_i q} \frac{\mu_p - \mu_n}{mu_p + mu_n} \tag{4.14}$$

In this case, when the value of R_H is positive, it means mobility of holes is larger than electrons and vice versa.

4.2.3 Hall Effect with Large Hall Angle

In reality, the tangent value of θ_H may greater than 1 because of the large mobility or strong magnetic field, then it is necessary for finding the model with large hall angle. In this part, the assumptions are reduced to only one assummption, that is the mean free time of carriers are equal. For single type carrier, with analysis of forces of electrons under constant electric and magnetic field , we have

$$\begin{cases} \frac{dv_x}{dt} = -\frac{q}{m} E_x - \omega v_y \\ \\ \frac{dv_y}{dt} = -\frac{q}{m} E_y + \omega v_x \end{cases} \tag{4.15}$$

where $\omega = \frac{qB_z}{m}$, and m is the effective mass of electron.
With the definition of current density, $J_x = -qnv_x$ and $J_y = -qnv_y$, we have

$$\begin{cases} J_x = \frac{nq^2}{m}\left(\frac{\tau E_x}{1+\omega^2\tau^2} - \frac{\omega\tau^2 E_y}{1+\omega^2\tau^2}\right) \\ \\ J_y = \frac{nq^2}{m}\left(\frac{\tau E_y}{1+\omega^2\tau^2} + \frac{\omega\tau^2 E_x}{1+\omega^2\tau^2}\right) \end{cases} \tag{4.16}$$

where τ is the mean free time, which is the average interval between two scatterings, and its expression is $\tau = \frac{1}{\tau}\int_0^{infty} e^{-\frac{t}{\tau}dt}$. Since $J_y = 0$, we have

$$\frac{E_y}{E_x} = -\omega\tau \tag{4.17}$$

The hall angle is

$$tan(\theta_H) = -\omega\tau = -\frac{Bq\tau}{m} = -\mu_n B \tag{4.18}$$

Apply Eq (4.17) into Eq (4.16), we have

$$J_x = \frac{nq^2\tau E_x}{m} = nq\mu_n E_x = \sigma E_x \tag{4.19}$$

where $\mu = \frac{q\tau}{m}$, and we also have

$$R_H = -\frac{1}{nq} \tag{4.20}$$

Eq (4.18) and Eq (4.20) are the same with the case in small hall angle, which means the value of hall angle doesn't have an influence on its hall coefficient.

For two carrier model, the case is much more complicated. According to R.G.Chambers' article[3], Eq (4.16) can be refined as

$$\begin{cases} J_x = (A_1 + A_2)E_x - (D_1 + D_2)E_y \\ \\ J_y = (A_1 + A_2)E_y + (D_1 + D_2)E_x \end{cases} \tag{4.21}$$

Since the value of J_y is equal to zero, we have

$$E_x = -\frac{(A_1 + A_2)E_y}{D_1 + D_2} \tag{4.22}$$

Then we have the expression of R_H

$$R_H = -\frac{1}{B}\frac{D_1 + D_2}{(A_1 + A_2)^2 + (D_1 + D_2)^2} \tag{4.23}$$

In Eq (4.23), A_1, A_2, D_1 and D_2 can be expressed as the combination of magnetic field and resistance like $A_1 = \frac{\sigma_1}{1+\sigma_1^2 B^2 R_1^2}, D_1 = -\frac{\sigma_1^2 B R_1}{1+\sigma_1^2 B^2 R_1^2}$, and Eq (4.23) can be rewritten as

$$R_H = \frac{R_1\sigma_1^2(1 + \sigma_2^2 B^2 R_2^2)^2 + R_2\sigma_2^2(1 + \sigma_1^2 B^2 R_1^2)^2}{(\sigma_1 + \sigma_2)^2 + \sigma_1^2\sigma_2^2 B^2(R_1 + R_2)^2} \tag{4.24}$$

Then substitute σ_1, σ_2, R_1 and R_2 in Eq(4.24), we have

$$R_H = \frac{1}{q}\frac{(p - nb^2) + b^2\mu_p^2 B^2(p - n)}{(bn + p)^2 + b^2\mu_p^2 B^2(p - n)^2} \tag{4.25}$$

where $b = \frac{\mu_n}{\mu_p}$.

For Eq (4.25), the mean free time τ must be a constant. When the hall angle is small, say B is small enough, Eq (4.25) can be refined as $R_H = \frac{1}{q}\frac{p\mu_p^2 - n\mu_n^2}{(p\mu_p + n\mu_n)^2}$, which is the same with Eq (4.13), so Eq (4.25) is suitable for any hall angles. One notice is that in extremely large magnetic field, Eq (4.25) become

$$\lim_{B\to+\infty} R_H = \frac{1}{q(p-n)} \tag{4.26}$$

In this case, when the value of R_H is positive, it means carrier density of holes is larger than electrons and vice versa.

4.2.4 Hall Effect with Different Mean Free Time

In analysis above, the mean free time is a constant, however, in reality, because of the different scatterings in lattice, the mean free time of particles are different and have a relationship with their energy. In this part, cases with different mean free times will be discussed.

For electrons that hold an energy between E and $E + dE$, assume the quantity of them is $\Delta n(E)$, then the current density is

$$\Delta J = \frac{\Delta n(E) q^2 \tau(E)}{m} \tag{4.27}$$

Integrate ΔJ, we have

$$J = \frac{nq^2 < \tau >}{m} \tag{4.28}$$

where

$$< \tau >= \frac{\int_0^\infty EN(E)e^{-\frac{E}{kT}}\tau(E)dE}{\int_0^\infty EN(E)e * -\frac{E}{kT}dE} \tag{4.29}$$

Eq (4.29) is integrating the mean free time with different energy. $\tau(E)$ is the free time function with energy E, for different scatterings, the whole mean time follows the rule as $\frac{1}{\tau} = \frac{1}{\tau_1} + \frac{1}{\tau_2} + \frac{1}{\tau_3} + \cdots$ [1].

For Eq (4.16), take variable τ into account, it becomes to

$$\begin{cases} J_x = \frac{nq^2}{m}[< \tau > E_x - \omega < \tau^2 > E_y] \\ J_y = \frac{nq^2}{m}[< \tau > E_y - \omega < \tau^2 > E_x] \end{cases} \tag{4.30}$$

With the current in y-axis is zero, we can get the hall angle as

$$tan(\theta_H) = \frac{E_y}{E_x} = \frac{m\omega < \tau^2 >}{nq^2 < \tau >} \tag{4.31}$$

Eq (4.31) can be seen as the the original expression with a coefficient $\frac{<\tau^2>}{<\tau>^2}$

Then we have the hall coefficient as

$$R_H = -\frac{A}{nq}, A = \frac{< \tau^2 >}{< \tau >^2} \tag{4.32}$$

	τ is a constant	τ varies with energy
Single Carrier	$R_H = -\frac{1}{nq} or \frac{1}{pq}$	$R_H = -\frac{A}{nq} or \frac{A}{pq}$
Two Carriers & Small Hall Angle	$R_H = \frac{1}{q}\frac{p\mu_p^2 - n\mu_n^2}{(p\mu_p + n\mu_n)^2}$	$R_H = \frac{A}{q}\frac{p\mu_p^2 - n\mu_n^2}{(p\mu_p + n\mu_n)^2}$
Two Carriers & Large Hall Angle	$R_H = \frac{1}{q}\frac{(p-nb^2)+b^2\mu_p^2B^2(p-n)}{(bn+p)^2+b^2\mu_p^2B^2(p0n)^2}$	$R_H = \frac{A}{q}\frac{(p-nb^2)+b^2\mu_p^2B^2(p-n)}{(bn+p)^2+b^2\mu_p^2B^2(p0n)^2}$

Table 4.1: Hall coefficient in different situations

Since A is a funcion of τ, when the expression of τ is given, we can calculate the value of A. For example, for lattice scattering cases, $\tau = \alpha E^{-0.5}$, then we can get the value of A as $A = \frac{3\pi}{8}$ [5]. Further more, when the value of A is given, we may give the expression of τ and decide what kind of mechanism that causes the scattering.

In conclusion, for cases that mean free time is not a constant, there need a correction coefficient A, which is determined by the scattering mechanism and energy states distribution.

4.2.5 Conclusion of Hall Effect Model

This section gives a theoretical analysis of hall effect in different conditions. From the simplest case (single carrier, small hall angle, constant mean free time) to the most complicated case (two carriers, large hall ange, different mean free time), we correct the original expression of hall coefficient R_H. Table (4.1) gives the results we get in this chapter.

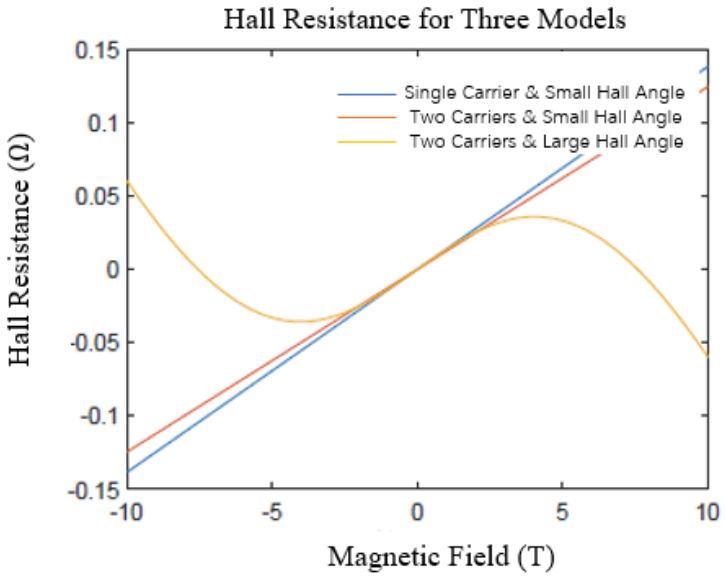

Figure 4.2: Hall resistance in different models

Figure (4.2) gives a general trend of hall resistance to magnetic field in three

models. For small hall angle cases, the curves are all straight lines, and the slope of single carrier model is smaller the two carriers model. For large hall angle case, the curve is non-linear with the magnetic field. For differenct mean free time, there introduce a correction coefficient A, where A is the correction coefficient for different mean free time, and it is equal to $\frac{<\tau^2>}{<\tau>^2}$.

4.3 Quantum Hall Effect & SdH Oscillation

The discovery of the quantum Hall effect (QHE) was the result of systematic measurements on the two-dimensional electron gas (2DEG) systems, where the electrons are free to propagate in the $x-y$ plane but are confined by some potential $U(z)$ along the z-direction. It is known that when a strong magnetic field is applied perpendicular to such 2DEG system, the Hamiltonian is described by:

$$\{-\frac{\hbar^2}{2m}\nabla^2+\frac{m\omega_c^2}{8}(x^2+y^2)-i\hbar\omega_c[x\frac{\partial}{\partial y}+y\frac{\partial}{\partial x}]\}\phi=E\phi \tag{4.33}$$

where $\omega_{\frac{eB}{m}}$ is the cyclotron frequency. Under such circumstances, the electron in the conduction band will behave like simple harmonic oscillator, and the eigenstates of energy, so-called Landau Levels (LLs), are quantized in the x-y plane as

$$E_n=E_0+(n+\frac{1}{2})\hbar\omega_c \tag{4.34}$$

where E_0 is the ground state determined by U(z). In such quantized LLs condition, it was first proposed by L.W Schubnikov and W.J de Haas that the longitudinal conductivity σ_{xx} would oscillate periodically with the change of applied magnetic field. Hall conductance σ_{xx} takes quantized values in different magnetic fields and its expression is

$$\sigma_{xx}=\nu\frac{e^2}{h} \tag{4.35}$$

where e is the elementray charge, h is Plank's constant and coefficient ν can take either integers like 1, 2, 3$\cdots$ or fractional values like $\frac{1}{3},\frac{2}{5},\frac{3}{7}\cdots$ [24]. Quantum Hall effect is referred as integer or fractional quantum Hall effect depending on whether the value of ν is an integer or a fractional number respectively.

In Figure (4.3), we can see that for hall resistance R_{xy}, they are quantized in different magnetic fields, which is the quantum hall effect and for magnetoresistance R_{xx}, they start oscillating and somehow the period of the oscillation is the same as the width of quantized plateau, which is SdH oscillation. According to the deduction by A.A.Taskin and Yoichi Ando[20], Rxx is proportional to $cos[2\pi(\frac{f}{B}-\phi)]$ where f is the frequency of the oscillation, ϕ is the phase. The corresponding Shubnikov-de Haas (SdH) oscillation period only depends on the carrier density n_{2D} in the 2DEG system:

$$f=\frac{1}{\delta\frac{1}{B}}=\frac{\hbar k_F^2}{2e}=\frac{n_{2D}h}{2e} \tag{4.36}$$

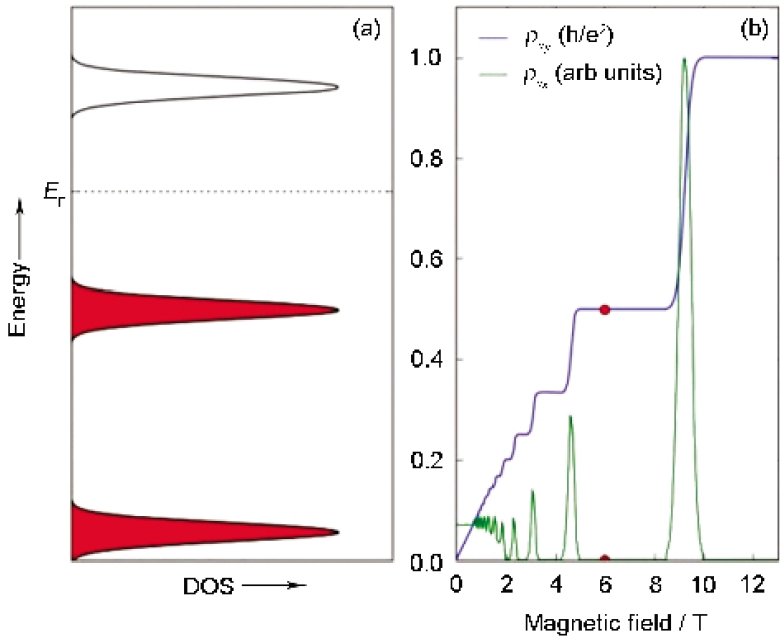

Figure 4.3: Quantum hall effect & SdH oscillation

where n_{2D} is the carrier density of 2-dimensional electron gas. One thing need to be noticed is this carrier density is for the carriers that are taking part in the oscillation other than the carriers that are conducting electricity. SdH oscillation can help to calculate the carrier density but it also has its weakness. SdH oscillation or quantum hall effect is hard to detect, the measured sample should be clean enough and since the oscillation signal is very tiny, the noise of measurement system should be highly precise.

For different kinds of materials, the frequencies of the oscillation are also different, finding the frequency of the oscillation will help to calculate the carrier density of the material and analyze other properties.

4.4 Summary

This chapter gives a theoretical analysis of hall effect in different conditions. From the simplest case to the most complicated case, we correct the original expression of hall coefficient R_H as the prerequisites are removed gradually. An general introduction of SdH oscillation and quantum hall effect is also given in this part. In next chapter, will verify the model proposed in this part and decide what improvement we can do in the future.

Chapter 5 Measurements & Analysis

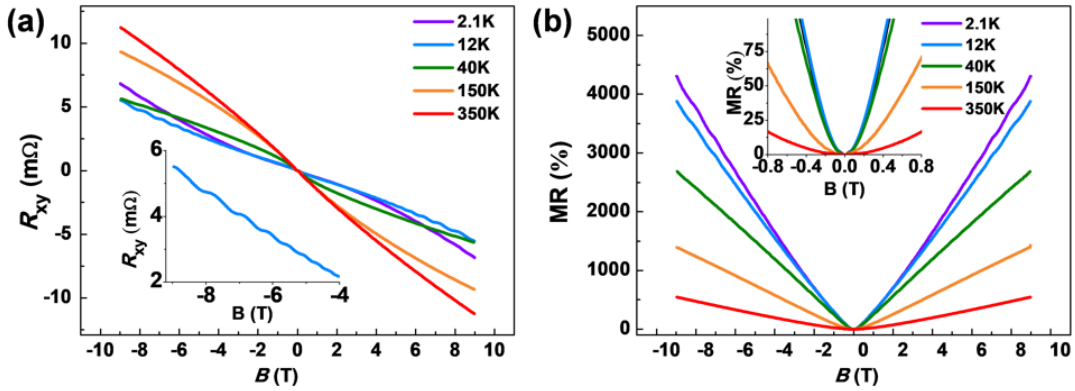

Figure 5.1: Temperature-dependent magneto-transport properties of the Cd_3As_2 sample. (a) Magnetic field-dependent Hall resistance R_{xy} at different temperatures. Non-linear features can be observed in all measured data. Inset: quantum oscillation of R_{xy} at $T = 12$K. (b) Magnetic field-dependent MR at different temperatures. Non-saturating linear MR background is found to persist up to 350 K. Inset: The evolution of the thermal broadening-induced parabolic MR around $B = 0$T.

In order to explore the electrical properties of the Cd_3As_2 sample, temperature-dependent magneto-transport measurements were carried out, and corresponding Hall and MR results are summarized in Fig (5.1). Consistent with previous reports[12], the Hall resistance R_{xy} exhibits an obvious non-linear feature from 2.1K to 350K, implying the presence of multiply conduction channels in the Cd_3As_2 sample. In the meanwhile, the longitudinal resistance R_{xx} shows a giant magnetoresistance of $5\times10^{3}\%$ at 2.1K, and the non-saturating linear MR background also persists up to 350K, except that the thermal broadening-induced parabolic MR around $B = 0$T becomes more pronounced at higher temperatures (Inset of Fig (5.1(b)))[9]. Additionally, when $T < 20$K, distinct quantum oscillations start to appear at high magnetic fields in both the R_{xy} (Inset of Fig (5.1(a))) and R_{xx} (it will be elaborated in Fig (5.5)), hence suggesting that the Cd_3As_2 sample may have a high intrinsic carrier mobility.

5.1 Verification of Two-Band Model

Based on the above observations, it is concluded that the magneto-transport characteristics of the high-mobility Cd_3As_2 sample studied in this paper cannot be portrayed by ordinary Hall model nor the conventional parabolic MR relations where the small-Hall-angle condition is assumed. Alternatively, in the general case, under the presence of a perpendicular magnetic field $\vec{B} = B_z \cdot \vec{z}$ and in-plane electric field $\vec{E} = E_x \cdot \vec{x} + E_y \cdot \vec{y}$ (i.e., $E_x \cdot \vec{x}$ is the longitudinal applied field while $E_y \cdot \vec{y}$ is the transverse induced field by Hall effect), the classic carrier motion (v_x, v_y) in the Hall-bar device can be rigorously described by $\dot{v_x} = -\frac{eE_x}{m^*} - \omega v_y, \dot{v_y} = -\frac{eE_y}{m^*} - \omega v_x$, where e is the electron charge, m^* is the electron effective mass, $\omega = \frac{eB_z}{m^*}$ is the cyclotron frequency, and in steady state, the Hall angle is found to be $\tan\theta_H = \frac{E_y}{E_x} = \mu \cdot B_z$ [4]. Given the multiple-channel conduction nature in this sample, we further adopted the generic two-band transport model in which the Hall resistance R_{xy} is determined by both E_x and E_y. (i.e., θ_H is not negligible)

$$R_{xy} = \frac{B}{e} \frac{(p - nb^2) + b^2\mu_p^2 B^2 (p - n)}{(bn + p)^2 + b^2\mu_p^2 (p - n)^2} \tag{5.1}$$

where $n(p)$ is the electron(hole) concentration, $\mu_n(\mu_p)$ is the electron(hole) mobility, and b is defined as $b = \frac{\mu_n}{\mu_p}$. It can be seen that under the small-Hall-angle condition where $\mu \cdot B_z \sim 0, Eq(5.1)$ would reduce to the conventional two-band model.

$$R_{xy} = \frac{B}{e} \frac{(p\mu_p^2 - n\mu_n^2}{(p\mu_p + n\mu_n)^2} \tag{5.2}$$

Besides, it is also noted that when the transport is governed by a single conduction channel, the ordinary Hall slope $(R_{xy} = -\frac{B}{en} or + \frac{B}{ep})$ could resume no matter whether θ_H is neglected or not.

Accordingly, by applying Eq (5.1) on our Cd_3As_2 sample, we managed to trace the R_{xy} data for all temperature sets with nominal R-squared values above 0.99, and Fig (5.2) illustrates the fitted data along with the measured values at $T = 2.1$K and 350K, respectively. It is clearly observed that both fittings can precisely capture each corresponding non-linear character of the $R_{xy} - B$ plot within the entire magnetic field range [-9T, +9T]. On the contrary, conventional two-band transport model, with the same numbers of fitting parameters (n, μ_n, p, μ_p), only managed to follow the low-field data (i.e., small-Hall-angle condition) while the fitting error was progressively amplified under high magnetic fields, as shown in Fig (5.2). Therefore, Fig (5.2) demonstrates the universality of the Large-Hall-angle two-band transport model.

Similarly, following the same carrier motion equation along the $x - y$ plane, we also obtained the general expression for the magnetoresistance under the fixed carrier lifetime [10].

$$\Delta R_{xx}(B) = R_{xx}(B) - R_{xx}(0) = \frac{npb\mu_p^2 (b + 1)^2}{(nb + p)^2 + (\mu_n - \mu_p)^2 b B^2} B^2 \cdot R_{xx}(0) \tag{5.3}$$

where $R_x x(0)$ is the longitudinal resistance at zero magnetic field, and the $(\mu_n - \mu_p)^2 b B^2$ is the correction term for giant-MR semimetal materials such like WTe_2 and

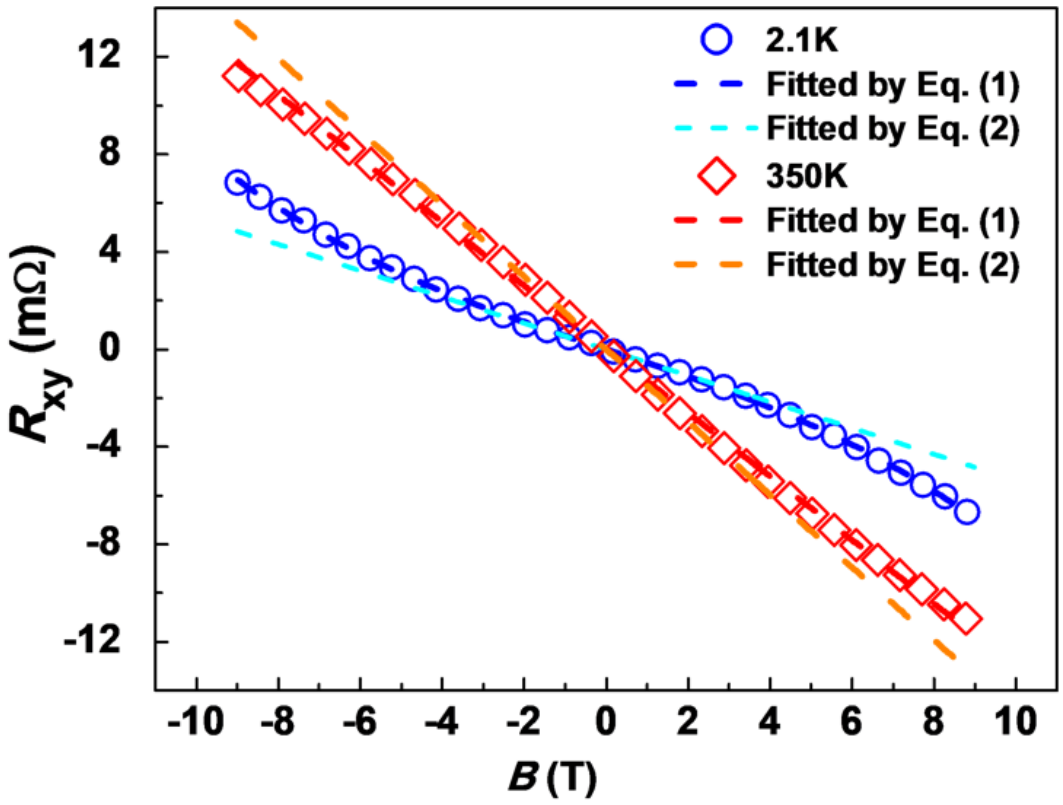

Figure 5.2: Fitting results of Rxy by Eq (5.1) at T = 2.1K and 350K, respectively. As a comparison, conventional two-band transport model Eq (5.2) only manages to fit the small magnetic field regime.

LaBi[18]. Fig (5.3) shows the well-fitted MR results of the Cd_3As_2 sample at T = 2.1K and 350K, respectively. Here, we need to point out that since the onset of the linear MR occurs at a small magnetic field possibly owing to the linear-band dispersion and concomitant Dirac fermions[20], we only applied Eq (5.3) within a relatively small magnetic field range of [-0.6T, +0.6T]. Nevertheless, given the large Hall angle $\theta_H \sim 60^\circ$ at $B = \pm 0.6T$ for the 2.1K data, we hence may conclude that Eq (5.3) can be used as the general form to reveal the magneto-transport behaviors of the high-mobility Cd_3As_2 sample under both the small-Hall-angle and the large-Hall-angle scenarios. In addition, it is also worthwhile to mention that our measured linear MR slopes at higher magnetic fields might correspond to the Weyl nodes-related mechanisms[25] [2], yet the underlying physics needs to be further justified.

5.2 Temperature-Mobility Analysis

In view of investigating the TDS insights of the Cd_3As_2 sample, three key parameters, namely the carrier concentrations (n, p) and electron mobility μ_n, were further

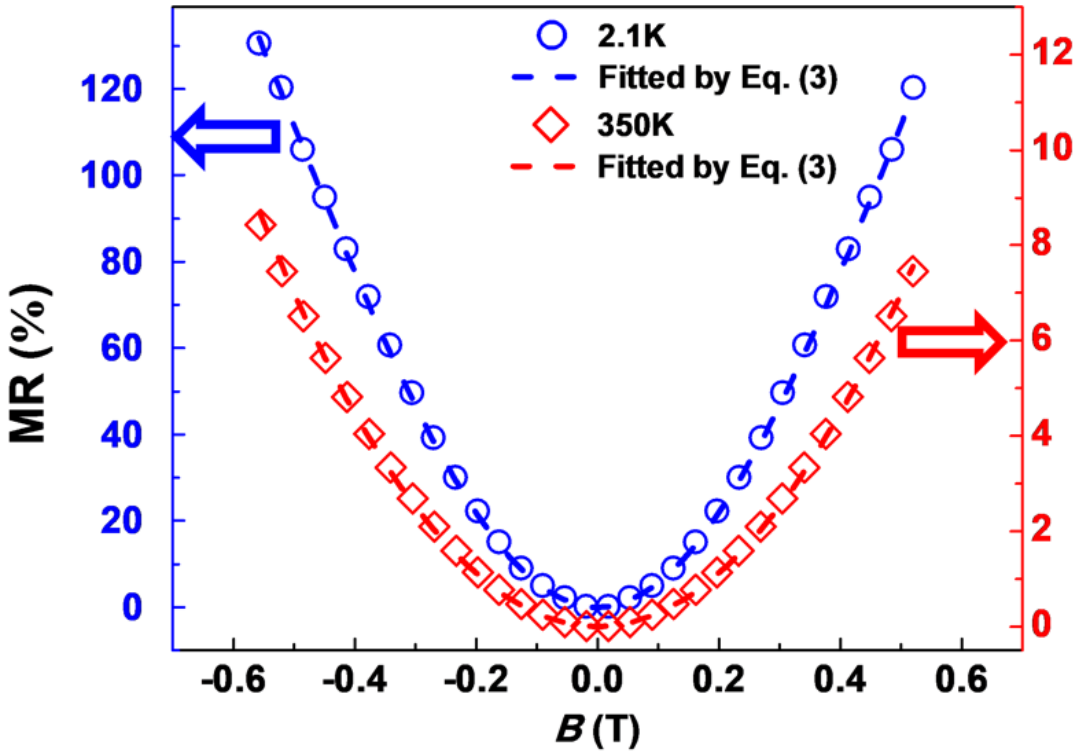

Figure 5.3: Fitting results of MR in the [-0.6T, +0.6T] range by Eq (5.3).

extracted from Fig (5.1), and their temperature-dependent results are plotted in Fig (5.4) (it is noted that the calculated hole mobility μ_p was too small as compared to μ_n, probably due to the small Fermi velocity of the Cd_3As_2 valence band. Hence, we did not include the μ_p data here). Based on the same magneto-transport mechanism employed in Eq (5.1) and (5.3), all these key parameters obtained from the R_{xy} and MR data all show high consistency within the whole temperature range, again validating the above proposed generic two-band transport model. Meanwhile, when lowering the temperature, both the electron and hole concentrations gradually increase until $T = 20$K. Coincidentally, the electron mobility is mainly limited by the strong phonon scattering within this temperature window (i.e., 20K $< T <$ 350K), as the temperature-dependent electron mobility can be well-explained by the following relation

$$\mu_n(T)^{-1} = A_1 \cdot T^{\frac{3}{2}} + A_2 \cdot [e^{\frac{\hbar\omega}{k_B T}} - 1]^{-1} \tag{5.4}$$

where A_1 and A_2 are the weighting coefficients, k_B is the Boltzmann constant, and $\hbar$ is the reduced Plank constant. The first term on the right-hand side of Eq (5.4) represents the acoustic phonon scattering while the second term relates to the optical phonon scattering. From the fitting result (gray dashed line) shown in Fig (5.4(c)), the relevant optical phonon frequency is calculated to be $\omega_1 = 2.66 \times 10^{12}$Hz(or 87cm^{-1}) whose magnitude is similar to that obtained from the Raman spectra. On the other hand, once the base temperature is below 20K, $\mu_n(T)$ fails to abide by Eq (5.4), indicating the presence of additional scattering mechanisms in such ultra-low temperature regime.[15]

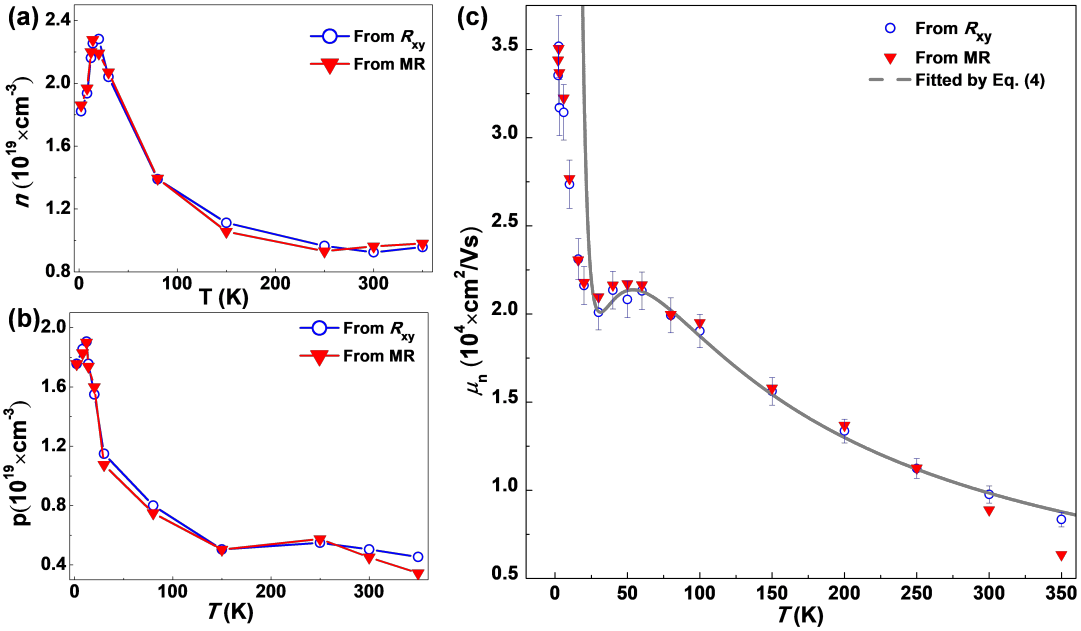

Figure 5.4: Temperature dependences of carrier concentrations and electron mobility of the Cd_3As_2 sample. All data are extracted from Fig (5.1) using the generic large-Hall-angle two-band transport model. When the sample is cooled down, the concentrations of (a) electron and (b) holes both gradually increase until $T < 20$K. (c) The temperature-dependent electron mobility can be explained by the phonon scatterings in the [20K, 350K] range, below which additional scattering mechanisms may appear.

5.3 SdH Oscillation Analysis

Subsequently, we continued to probe the unique 2D Fermi surface states of the Cd_3As_2 crystal through quantum oscillations[23]. Thanks to the high-mobility (i.e., μ_n is already larger than 10^4cm$^2/V{\cdot}s$ at room temperature and monotonically increases to $3.44{\times}10^4 cm^2/V{\cdot}s$ at 2.1K) and the resultant large Hall angle, the system is driven into the quantum transport regime when $B > 4$T, and pronounced SdH oscillations can be observed up to $T = 20$K.

The SdH oscillation amplitude [$\Delta R_{xx} = R_{xx} - < R_{xx} >$] is obtained by subtracting a smooth non-oscillatory background $< R_{xx} >$ from the oscillating R_{xx} and plotted against the inverse magnetic field in the inset of Fig (5.5(a)). Regardless of the temperature variations, all the SdH oscillation data exhibit a single frequency of $F = 64.1$ T (i.e., the periodicity is $\Delta(\frac{1}{B}) = 0.0156T^{-1}$) which is identified from the fast Fourier transform spectra (Inset of Fig (5.5(a))).

For SdH oscillation, the frequency F is proportional to the cross-section area of the Fermi surface (S_F) that is normal to the magnetic field and can be described by

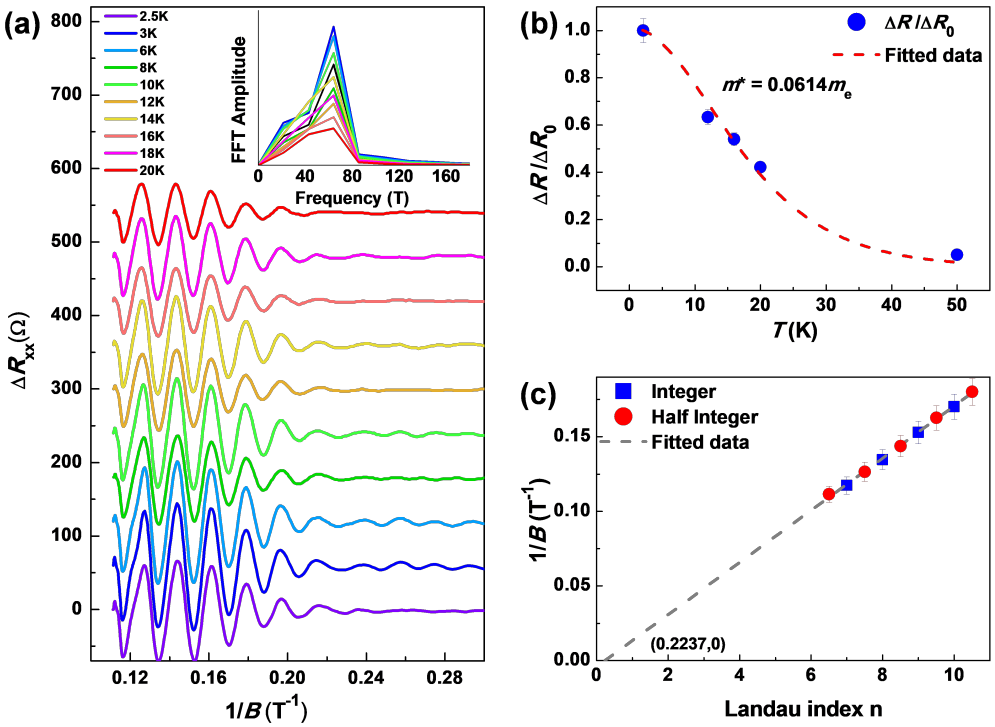

Figure 5.5: Magneto-transport properties of the Cd_3As_2 sample in the quantum transport regime. (a) Temperature-dependent Shubinikov-de Haas oscillations. The positions of all ΔR_{xx} peaks and valleys remain the same from 2.1K to 20K. Linear MR backgrounds are subtracted and the data are shifted vertically for convenient comparison. Inset: the fast Fourier transform spectra identify a single oscillation frequency of f = 64.1T. (b) The temperature dependence of normalized oscillation amplitude $\frac{\Delta R_{xx}(T)}{\Delta R_0}$ where ΔR_0 is defined as ΔR_{xx}(2.1 K). The solid line is the best fit to the Lifshitz-Kosevich formula and the cyclotron effective mass is calculated to be $m^* = 0.061 m_e$. (c) The Landau index n versus $\frac{1}{B}$. The integer (ΔR_{xx} valleys in Fig (5.5(a))) and half-integer indices (ΔR_{xx} peaks in Fig (5.5(a))) fall into a straight line with the n-axis intercept corresponding to a non-zero Berry phase of (0.56±0.06) π.

the Onsager relationship[7]. From the Onsager relation $F = \frac{\Phi_0}{2\pi^2} S_F$ with the magnetic flux quantum $\Phi_0 = \frac{h}{2e}$, the cross-sectional area of the Fermi surface normal to the field is determined as $S_F = 6.14 \times 10^{-3} \dot{A}^{-2}$, which in turn gives the value of the Fermi momentum $k_F \approx 0.044 \dot{A}^{-1}$.

In the meanwhile, Following the Lifshitz-Kosevich (LK) theory, the amplitude of $\Delta R_{xx}(T)$ can be described by $\Delta R_{xx} \propto \frac{\sinh \lambda(T)}{\lambda(T)} e^{-\lambda(T)}$ where $\lambda(T) = 2\pi^2 k_B T m_{cyc} \hbar e B$

is the thermal factor and m_{cyc} is the cyclotron mass. Therefore, by applying the best fitting, we are able to obtain a rather small $m_{cyc} = 0.058m_e$ and its corresponding Fermi velocity $v_F = \frac{\hbar k_F}{m_{cyc}} = 8.8 \times 10^5 m/s$.

Finally, the Landau index plot of the Cd_3As_2 sample is provided in Fig (5.5(c)) where the peaks and the valleys of ΔR_{xx} (i.e., the half-integer and the integer index respectively) follow a straight line with respect to $\frac{1}{B}$, and the Landau index n-axis intercept of Fig (5.5(c)) may imply the presence of the non-zero Berry phase of $2\pi\beta = (0.56 \pm 0.06)\pi$ in the Cd_3As_2 sample, and our results are similar to previous reports.

5.4 Summary

In summary, we have studied the magneto-transport properties of the bulk Cd_3As_2 sample. Given the high electron mobility in such system, we applied a large-Hall-angle two-band transport model to describe both the longitudinal and Hall resistances from 2.1K to 350K, and found the surface-dominated conduction with unconventional scattering mechanisms may occur when the based temperature is below 20K. At the same time, the large Hall angle of the sample also enabled us to observe distinct SdH oscillations under relative small magnetic fields as well as to reveal non-trivial quantum transport features at low temperatures. Our work thus offers an effective method to understand these exotic topological transport phenomena and the underlying physics, which may further unveil new application opportunities for novel topological quantum materials.

Bibliography

[1] *Semiconductor Physics And Devices*. Irwin, 1992.

[2] A. A Abrikosov. Quantum magnetoresistance. *Physical Review B*, 58(5):2788–2794, 1998.

[3] R. G. Chambers. The Two-Band Effect in Conduction. *Proceedings of the Physical Society A*, 65:903–910, November 1952.

[4] T. R. Chien, Z. Z. Wang, and N. P. Ong. Effect of zn impurities on the normal-state hall angle in single-crystal $\mathrm{yba_2cu_{3-x}zn_xo_{7-\delta}}$. *Phys. Rev. Lett.*, 67:2088–2091, Oct 1991.

[5] E. M. Conwell. Properties of silicon and germanium. *Proceedings of the IRE*, 40(11):1327–1337, 1952.

[6] A. B. Fowler, F. F. Fang, W. E. Howard, and P. J. Stiles. Magneto-oscillatory conductance in silicon surfaces. *Phys. Rev. Lett.*, 16:901–903, May 1966.

[7] Lei Guo, Yu-Kuai Liu, Guan-Yin Gao, Ye-Yu Huang, Heng Gao, Lei Chen, Weiyao Zhao, Wei Ren, Shi-Yan Li, Xiao-Guang Li, Shuai Dong, and Ren-Kui Zheng. Extreme magnetoresistance and sdh oscillation in compensated semimetals of nbsb2 single crystals. *Journal of Applied Physics*, 123(15):155103, 2018.

[8] E. H. Hall. On a new action of the magnet on electric currents. *American Journal of Mathematics*, 2(3):287–292, 1879.

[9] L. P. He, X. C. Hong, J. K. Dong, J. Pan, Z. Zhang, J. Zhang, and S. Y. Li. Quantum transport evidence for the three-dimensional dirac semimetal phase in $\mathrm{cd_3as_2}$. *Phys. Rev. Lett.*, 113:246402, Dec 2014.

[10] A. H. Kahn. Electrons and phonons. the theory of transport phenomena in solids by j. m. ziman. *Sririajmedj Com*, 133, 1960.

[11] C. A. Kittel. Introduction to solid state physics (app. a). *American Journal of Physics*, 21(8):547–548, 1954.

[12] He Liang, Xiu Faxian, Yu Xinxin, Teague Marcus, Jiang Wanjun, Fan Yabin, Kou Xufeng, Lang Murong, Wang Yong, Huang Guan, Yeh Nai-Chang, and Wang Kang L. Surface-dominated conduction in a 6 nm thick bi2se3 thin film. *Nano Letters*, 12(3):1486–1490, 2012. PMID: 22316380.

[13] Z. K. Liu, J. Jiang, B. Zhou, Z. J. Wang, Y. Zhang, H. M. Weng, D. Prabhakaran, S. K. Mo, H. Peng, P. Dudin, T. Kim, M. Hoesch, Z. Fang, X. Dai, Z. X. Shen, D. L. Feng, Z. Hussain, and Y. L. Chen. A stable three-dimensional topological dirac semimetal cd3as2. *Nature Materials*, 13:677, 2014.

[14] Madhab Neupane, Su-Yang Xu, Raman Sankar, Nasser Alidoust, Guang Bian, Chang Liu, Ilya Belopolski, Tay-Rong Chang, Horng-Tay Jeng, Hsin Lin, Arun Bansil, Fangcheng Chou, and M. Zahid Hasan. Observation of a three-dimensional topological dirac semimetal phase in high-mobility cd3as2. *Nature Communications*, 5:3786, 2014.

[15] S.Das Sarma and E.H Hwang. Interface-charged impurity scattering in semiconductor mosfets and modfets: temperature-dependent resistivity and 2d 'metallic' behavior. *Superlattices & Microstructures*, 27(5-6):421–424, 2000.

[16] E. Schrödinger. An Undulatory Theory of the Mechanics of Atoms and Molecules. *Physical Review*, 28:1049–1070, December 1926.

[17] R.A. Smith. *Semiconductors*. University Press, 1961.

[18] Shanshan Sun, Qi Wang, Peng Jie Guo, Kai Liu, and Hechang Lei. Large magnetoresistance in labi: origin of field-induced resistivity upturn and plateau in compensated semimetals. *New Journal of Physics*, 18(8), 2016.

[19] S.M. Sze. *Physics of semiconductor devices*. Wiley international edition. Wiley-Interscience, 1969.

[20] A. A. Taskin and Yoichi Ando. Berry phase of nonideal dirac fermions in topological insulators. *Phys. Rev. B*, 84:035301, Jul 2011.

[21] L. J. van der PAUW. *A method of measuring spesific resistivity and hall effect of discs of arbitrary shape*, pages 174–182. WORLD SCIENTIFIC, 2017.

[22] Xiangang Wan, Ari M. Turner, Ashvin Vishwanath, and Sergey Y. Savrasov. Topological semimetal and fermi-arc surface states in the electronic structure of pyrochlore iridates. *Physical Review B*, 83(20):205101, 2011.

[23] Feng Ya, Wang Zhijun, Chen Chaoyu, Shi Youguo, Xie Zhuojin, Yi Hemian, Liang Aiji, He Shaolong, He Junfeng, and Peng Yingying. Strong anisotropy of dirac cones in srmnbi2 and camnbi2 revealed by angle-resolved photoemission spectroscopy. *Sci Rep*, 4:5385, 2013.

[24] D.R. Yennie. Integral quantum hall effect for nonspecialists. *Reviews of Modern Physics*, 59(3):781–824, 1987.

[25] Wang Zhijun, Weng Hongming, Wu Quansheng, Dai Xi, and Fang Zhong. Three-dimensional dirac semimetal and quantum transport in cd 3 as 2. *Phys.rev.b*, 88(12):13235–13241, 2013.

Acknowledgment

First of all, I would like to express my sincere gratitude to Progessor Kou Xufeng for his support of my study and research. Since I entered TALENT group at Feb 2017, Professor Kou helped and guided me a lot. And I will never forget the days I worked with him. His guidance helped me in all the time of research and completion of this thesis.

Secondly, I would say thank you to all the fellows in TALENT group including Liu Xiangyang, Gu Yi, Zhang Yong, Wang Zewei and Li Jiaming, who are graduate students in TALENT. They shared a lot of experience in science research with me during the days I worked with them.

Last but not least, I would say thank you to my parent, who supported everything in my life so that I could focus on my research.